The 27–28 October 1986 FIRE IFO Cirrus Case Study: Cloud Parameter Fields Derived from Satellite Data

PATRICK MINNIS,* PATRICK W. HECK† AND EDWIN F. HARRISON*

*Atmospheric Sciences Division, NASA Langley Research Center, Hampton, Virginia
†Lockheed Engineering and Sciences Company, Hampton, Virginia

(Manuscript received 18 May 1987, in final form 26 February 1990)

ABSTRACT

A methodology for estimating cirrus cloud amounts and altitudes using visible and infrared satellite data was developed and tested using FIRE Cirrus Intensive Field Observation (IFO) coincident lidar and satellite data with a theoretical cloud albedo model. On average, cloud center heights could be determined to within ±0.9 km of the lidar-derived values using the satellite data alone. Satellite-derived, total cloud tops are generally 0.5 ± 0.9 km lower than the lidar cloud tops. If only high clouds are considered, the average cloud top is 0.1 ± 0.6 km higher than the lidar cloud top. The accuracies of the lidar cloud-center and cloud-top heights are estimated to be within ±0.7 km of the actual values. Satellite-derived average cloud emittance and visible optical depths can be determined to within ±0.05 and ±0.13, respectively, of the reference cloud emittance. Cirrus cloud thickness was also derived. The satellite retrieval yields cloud depths that are 0.3 ± 1.0 km thinner than the lidar-derived cloud thicknesses. The accuracy of the lidar-derived cloud depths is estimated to be 0.7 km. It was concluded that compared to a method which analyzes each pixel individually, a bispectral approach, which averages some of the pixel values before analysis, yields lower rms and bias errors in some of the derived parameter values.

The technique was applied to GOES and AVHRR data taken during the daylight hours of the FIRE Cirrus IFO case study on a 0.5° grid covering most of Wisconsin. Broadband radiation fields from the ERBE corresponding to the AVHRR results were also analyzed. During the afternoon of 27 October 1986, a cirrus field was tracked with the GOES data as it developed over northern Wisconsin. The satellite analyses revealed average cloud-top heights ranged between 9 and 11 km. Decreases in the outgoing longwave fluxes caused by the cloud appeared to be balanced by increases in the cloud albedo resulting in a negligible change in energy balance at the top of the atmosphere due to the cloud. During 28 October, the cloud fields were highly variable with both cirrus and midlevel clouds. An organized cirrus "wedge" developed and passed though the region during the middle of the day with cloud-top heights greater than 11 km. In addition to other cirrus clouds, an apparent cirrus convective complex passed through central Wisconsin during the afternoon with cloud tops between 10.0 km and the tropopause at ~11.3 km. A north–south line of clearing with scattered altocumulus separated the morning and afternoon cloud fields. This paper provides a comprehensive, quantified description of the case study clouds and should be useful for verifying ISCCP results and for improving the understanding of cirrus processes when combined with other IFO measurements.

1. Introduction

The Cirrus Intensive Field Observation (IFO) phase of the First ISCCP (International Satellite Cloud Climatology Project) Regional Experiment (FIRE) measured various properties of cirrus clouds using instruments on a range of platforms (see Starr 1987). Surface and aircraft observations provide small-scale point and line measurements of advecting and evolving cloud systems. Satellite radiance data provide a source for complete areal measurement of meso- and large-scale cirrus parameters. Ideally, the detailed cloud properties derived from the small-scale measurements need to be tied to the bulk cloud characteristics, which are typically derived from satellite data. Full linkage of all datasets for a comprehensive description of a given cloud field—one of the goals of the FIRE—should lead to significant progress in understanding, measuring, and modeling cirrus cloud systems.

Another purpose of the FIRE is validation of the ISCCP products (Rossow et al. 1988) and the methodology used to derive them and the development of improved cloud retrieval algorithms. Since the ISCCP products are based on 3-hourly satellite radiance data, typically, 8-km pixels sampled every fourth line and element, it is difficult to properly validate the ISCCP results using small-scale measurements taken on earth-bound platforms. If one means to overcome the time and space sampling mismatches between the ISCCP and the IFO, then one is to first establish relationships between the small-scale data and coincident, collocated satellite data. The relationships may then be applied

Corresponding author address: Patrick Minnis, Atmospheric Sciences Division, NASA/Langley Research Center, Hampton, VA 23665-5225.

to satellite data covering a larger area. The results of that application may be directly compared to the ISCCP products to assess their accuracies.

This paper documents a cirrus parameter retrieval methodology and the results of its application over the cirrus IFO area using data from the Geostationary Operational Environmental Satellite (GOES) taken during the FIRE cirrus case study days, 27–28 October 1986. Similar results computed from the NOAA-9 AVHRR (Advanced Very High Resolution Radiometer) and ERBE (Earth Radiation Budget Experiment) scanner data are also presented. The cloud properties determined here are primarily based on models developed from surface and airborne IFO measurements and coincident satellite data. The analyzed fields may be used to characterize the mesoscale variations in cirrus properties over the IFO area. Since these results are linked to the small-scale data, they may also be used as an initial validation set of cirrus cloud amounts and radiative properties for ISCCP products.

2. Data

a. GOES radiances

Half-hourly visible (VIS, 0.65 μm) and infrared (IR, 11.5 μm) radiances taken by the GOES located at ~98°W constitute the primary dataset. The IR pixels have a nominal resolution of 4 km × 8 km, while the VIS data are taken at 1 km. Normally, field-of-view matching was accomplished by averaging the VIS data up to 4-km × 4-km pixels and repeating every IR scan line to obtain effective 4-km × 4-km IR pixels. Because of collection problems, however, the data were obtained from two sources. The data from the secondary source were already averaged to a nominal 8-km resolution. Thus, 4-km data were used for some times while 8-km data were used for others. Since bispectral cirrus parameter retrievals require VIS data, only daytime data are analyzed here. The nominal calibration of the IR channel was used to convert the IR counts (0–255) to equivalent blackbody temperature, T. The VIS counts, D (0–63) were converted to reflectance using the calibration of C. H. Whitlock (1989, personal communication). That calibration yields the reflectance, $\rho = \{0.1624D^2 - 8.3\}/(526.9\ \mu_0)^{-1}$, where $\mu_0 = \cos\theta_0$ and θ_0 is the solar zenith angle. The GOES data were navigated as in Minnis and Harrison (1984a).

1) ANALYSIS GRID

A 0.5° × 0.5° analysis grid was used for the greater IFO area, defined here as the area between 42°N and 47°N latitudes and 87°W and 92°W longitudes. This area includes the IFO ground sites near its center. Two-dimensional histograms of VIS–IR pixel pairs were constructed from the data in each of the 0.5° regions. These histograms, stored in terms of VIS counts and IR temperatures, are then analyzed to derive cloud parameters for each region. Relative azimuth and viewing zenith angles, ψ and θ, respectively, along with the solar zenith angle were determined for the centers of each region.

2) DATA COMPRESSION

To efficiently store the histograms, the data are degraded in radiance precision before being packed into the histograms. This degradation is based on a division of the full 63 × 256 array of potential pixel pair values into nine zones as shown in Fig. 1. Because of minimal information content, pixels having $D < 4$, zone I, are eliminated. For GOES-6 during October 1986, the offset VIS count was ~7, so no pixels were included in this category. Means and standard deviations of D and T, and the number of pixels are the only quantities retained for zones II, VI, VII, VIII, and IX. Zone IX does not include $D = 49$. The original VIS precision is retained for the remaining sectors III, IV, and V. In zones III and V, the original thermal precision is degraded from 0.5 K to 1 K, while the original 0.5 K precision is retained for 300 K $\leq T <$ 264 K in zone IV. This data degradation scheme was designed to retain as much information as possible in most of the situations requiring high precision for cloud detection while enabling the extraction of histograms for a large number of regions in a single computer run on a given image. While this packing technique is suitable for low-level clouds over the ocean, it may present problems for distinguishing cold clouds over frigid surfaces ($T < -31$°C). Unless noted otherwise, all satellite data analyzed in this study have been compressed as outlined above.

b. AVHRR radiances

Global Area Coverage (GAC), 4-km data from the corresponding channels of the AVHRR were reduced

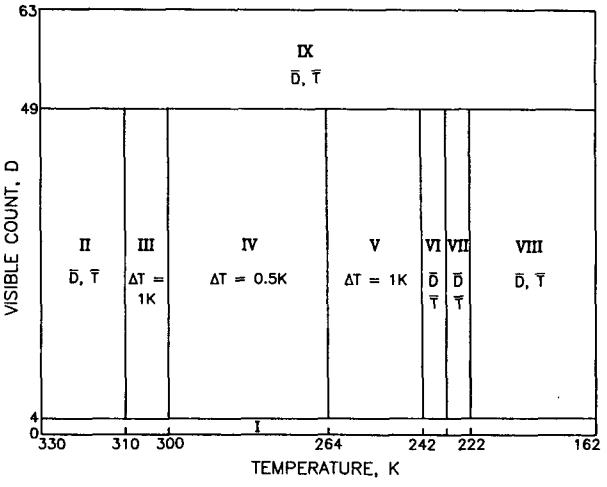

FIG. 1. Schematic bispectral histogram illustrating pixel compression categories.

in a similar fashion. The VIS data (channel 1) were converted to reflectance with the calibration given by C. H. Whitlock (1989, personal communication) where

$$\rho = \frac{(0.6060 D_A - 22.0)}{519.4/\mu_0}$$

and D_A is the AVHRR 10-bit count. The nominal count-to-temperature conversions were applied to channels 4 (11.2 μm) and 5 (12.2 μm). The resulting temperatures were averaged together to obtain a single temperature corresponding to that for the GOES 11.5-μm channel. The GOES-equivalent VIS–IR pixel pairs were then navigated with the nominal GAC navigation points and used to construct two-dimensional histograms for the 0.5° regions within the greater IFO area. The NOAA-9 IFO-area overpasses occurred at approximately 1930 UTC and 2100 UTC during 27 and 28 October, respectively.

c. *ERBE data*

The ERBE scanning radiometer on the NOAA-9 satellite has a nadir resolution of ~54 km and measures longwave, 5.0–50.0 μm, and shortwave, 0.2–5.0 μm, radiances as it scans the Earth in a cross-track direction. The radiances for each pixel are converted to longwave flux, M_{lw}, and shortwave albedo, α_{sw}, using the inversion process described by Smith et al. (1986).

d. *Temperature profiles*

Soundings taken every six hours over Green Bay, Wisconsin, were used to determine the vertical temperature structure of the atmosphere during the case study days. Linear interpolation between the sounding times was used to estimate the temperatures at each half hour.

e. *Lidar-satellite data*

The case study satellite and lidar datasets used by Minnis et al. (1990; hereafter, MYSAG) to determine cloud physical and radiative properties are also used here to evaluate the cloud height retrieval schemes. The satellite data are histograms constructed from strips of GOES data taken over several surface lidar sites. These strips correspond to the passage of clouds over the sites during a half-hour period. The lidars were used to determine the mean half-hour cloud-top and center altitudes as well as cloud thickness. More details of this dataset are given by MYSAG.

3. Methodology

a. *Basic procedures*

The parameters of interest here are cloud amount, C; cloud-top temperature, T_t; cloud-center temperature, T_c; cloud-top height, z_t; cloud-center height, z_c; cloud thickness, h; cloud emittance, ϵ; and VIS optical depth, τ_v. The relationships between these parameters during the IFO were explored by MYSAG using a limited dataset representing point and line samples. The results derived from that study are used here to determine values for each parameter from the observed radiance data over the greater IFO area during the case study period.

1) CLOUD VISIBLE OPTICAL DEPTH

When a measurement is determined to be from a cloudy area, it is assumed that the observed bidirectional reflectance,

$$\rho = \Upsilon_a \chi_c \alpha_c + \Upsilon_c \Upsilon_u \rho_s + \alpha_{sd}(1 - \alpha_d)(1 - \Upsilon_c - \alpha_c), \quad (1)$$

where the cloud albedo is $\alpha_c(\tau_v, \mu_0)$, the diffuse cloud albedo is $\alpha_d(\tau_v)$, and the cloud anisotropic reflectance factor is $\chi_c(\theta_0, \theta, \psi)$. The transmittance of the atmosphere due to ozone above the cloud is Υ_a (see MYSAG). The transmittances of direct downward and upward VIS radiation are $\Upsilon_c = \exp(-\tau_v/2\mu_0)$ and $\Upsilon_u = \exp(-\tau_v/2\mu)$. Clear-sky reflectance at time, t, is

$$\rho_s = \chi_s(\mu_0, \theta, \psi)\alpha_s(\lambda, \phi, t, \mu_0), \quad (2)$$

where χ_s is the clear-sky anisotropic reflectance factor, α_s is clear-sky albedo, λ is latitude, and ϕ is longitude. The diffuse clear-sky albedo, α_{sd}, is estimated with $\alpha_s(\lambda, \phi, \mu_0 = 0.55)$. For additional details regarding this parameterization, see MYSAG.

The values of $\alpha_c(\tau_v, \mu_0)$ taken from Takano and Liou (1989b) are based on radiative transfer calculations for a plane-parallel cloud composed of hexagonal columns with a length of 125 μm and width of 50 μm. Diffuse cloud albedo was determined as in MYSAG. Anisotropic reflectance factors for water, land, and low clouds are taken from the bidirectional reflectance models of Minnis and Harrison (1984b). In order to tie this analysis to the lidar sites, the anisotropic reflectance factors used for middle and high clouds were derived from the adjusted values of χ_c and χ_c', taken from the results of MYSAG. The MYSAG case study values of χ_c' derived over each lidar site were averaged for each hour and smoothed to obtain the values used here (Table 1). These results, constant for a given UTC, are used on the assumption that the viewing and illumination conditions over the greater IFO area do not differ significantly from those observed over the IFO lidar sites.

Clear-sky reflectances were derived on a 0.01° latitude–longitude grid using 1-km GOES VIS data during clear days in October 1986. Most of the data were taken during 19 October. These reflectances were converted to albedo with (2), then averaged to obtain a mean value of α_s at each half hour for every 0.5° grid box. For a given reflectance measurement, (1) is solved it-

TABLE 1. Anisotropic reflectance factors for clouds of different heights from GOES over IFO area during the case study.

Time (UTC)	χ_c (low)	χ_c' (mid-high)
1330	0.815	0.571
1400	0.854	0.673
1430	0.888	0.850
1500	0.922	0.900
1600	0.976	1.000
1700	1.016	1.205
1800	1.050	1.573
1900	1.028	1.289
1930	1.005	1.225
2000	0.982	1.097
2030	0.953	0.992
2100	0.919	0.915
2130	0.878	0.734
2200	0.835	0.563

eratively for τ_v using an average ozone abundance of 0.32 cm-STP (MYSAG), the clear-sky data, and the model results of Takano and Liou (1989b) described above.

2) CLOUD CENTER TEMPERATURE AND INFRARED EMITTANCE

Neglecting scattering, the infrared radiation emanating from the top of the cloud is the combination of absorptions and emissions at the various levels and temperatures within the cloud with the radiation that enters the cloud's base and passes unattenuated through the cloud. The radiance observed by the satellite over the cloud may be divided into two radiances: one that passes through the cloud and one that is emitted by the cloud. Since the actual vertical profiles of particle density and temperature within the cloud are unknown, it is necessary to characterize the cloud in terms of an equivalent radiating temperature, which is designated the cloud-center temperature, T_c. The correspondence of T_c to a geometrical location in the cloud depends on the vertical profiles of the cloud's microphysics and temperatures. It does not necessarily refer to the physical center of the cloud in the vertical.

The radiance emitted by the cloud then is $\epsilon B(T_c)$ and the radiance passing through the cloud is $(1 - \epsilon)B(T_{cs})$, where the infrared beam emittance ϵ is defined in terms of the cloud-center temperature, T_{cs} is the clear-sky temperature, and B is the Planck function at 11.5 μm. This formulation assumes that there is negligible attenuation of the radiance above the cloud. Assuming that a pixel with observed temperature T is completely cloud-filled, the cloud-center temperature is

$$T_c = B^{-1}\{[B(T) - (1 - \epsilon)B(T_{cs})]/\epsilon\}. \quad (3)$$

The clear-sky temperature is estimated as in Minnis et al. (1987). The inverse Planck function at 11.5 μm is denoted as B^{-1}. The infrared beam emittance is

$$\epsilon = 1 - \exp(-\tau_e/\mu), \quad (4)$$

where τ_e is the infrared optical depth. Its value is determined from the visible optical depth by inverting the relationship discussed by MYSAG. That is,

$$\tau_e = \tau_v/\xi, \quad (5)$$

where ξ is the mean scattering efficiency as defined by MYSAG. The mean value of $\xi = 2.17$ derived by MYSAG for the case study time period is used here. Thus, the value of τ_v is determined for a given measurement, then used with (5) to estimate τ_e. The emittance is computed with (4) and T_c is then derived with (3).

3) CLOUD-TOP TEMPERATURE

The vertical location of the physical top of the cloud is also estimated here. MYSAG found a strong correlation between the emittances derived using T_c and the actual cloud-top temperature, T_t, for temperatures below 253 K. Using linear regression on the data from Fig. 15 of MYSAG, it was found that the cloud-top emittance is

$$\epsilon_t = \epsilon(2.966 - 0.009141T_c). \quad (6)$$

Following (3), the cloud-top temperature is

$$T_t = B^{-1}\{[B(T) - (1 - \epsilon_t)B(T_{cs})]/\epsilon_t\}. \quad (7)$$

Equation (6) only holds for 217 K $\leq T_c \leq$ 253 K. For $T_c <$ 217 K, $\epsilon_t = 0.98\epsilon$, the solution to (6) for 217 K. For warm clouds with $T_c >$ 253 K, T_t is found from cloud thickness calculations. It is assumed that $z(T_c) = z(T_t) - 0.67h$, where h is the cloud depth. Although this approach for warm clouds is somewhat arbitrary, it affects few of the clouds of concern here.

4) CLOUD THICKNESS

MYSAG found that the cloud depth was related to the cloud-center temperature and the visible optical depth. Using their case study results in a multiple regression analysis, it was found that cloud thickness in km may be parameterized as

$$h = -14.8 + 0.076T_c + 0.467 \ln\tau_v,$$

if $T_c \leq$ 253 K. No data were available from their study for warmer clouds. To compute cloud thickness for $T_c >$ 253 K, a regression analysis was applied to the IR volume absorption coefficient data reported by Platt et al. (1987) to obtain

$$\sigma_a = 2.27 \times 10^{-8} \exp(0.068T_c).$$

The warm cloud thickness then is

$$h = \tau_e/\sigma_a.$$

The minimum and maximum thicknesses allowed for the warm clouds are 0.2 km and 3.0 km, respectively.

b. Layer processing

The system of equations defined above may be applied to a histogram yielding a cloud optical depth, emittance, height, and thickness for each pixel as in the ISCCP algorithm (Rossow et al. 1988). As noted in MYSAG, there is considerable pixel-to-pixel variability in these parameters due to variations in scattering properties and cloud shading. In order to minimize these effects, the data are preprocessed to compute an average temperature for each discrete reflectance in a given layer. This approach is similar to that used by MYSAG to perform the inverse analysis. The preprocessing and subsequent analysis are described below.

1) LAYER BOUNDARIES

Given the relationships between cloud reflectance and emittance, it is possible to define the potential observations for a cloud having the center temperature, T_c, with some function in terms of D and T. This function, $T_\epsilon(D)$, is given by a set of count-temperature pairs for discrete data. Since emittance depends on reflectance, a unique value of emittance, $\epsilon(D)$, may be determined for each discrete reflectance, $\rho(D)$, by finding τ_v with (1), computing τ_e from (3), and solving (4). For a given count, the temperature corresponding to a cloud-center temperature of T_c is

$$T_\epsilon = B^{-1}\{\epsilon(D)B(T_c) + [1 - \epsilon(D)]B(T_{cs})\}. \quad (8)$$

Solution of (8) over all observed count values defines the potential observations for a cloud having the center temperature, T_c, and the optical properties implied by the bidirectional reflectance model.

Following the practice of earlier cloud retrieval algorithms (e.g., Minnis et al. 1987; Stowe et al. 1988), the troposphere is divided into three layers: low, middle, and high, defined by the altitudes: $z < 2$ km, $2 \leq z < 6$ km, and $z \geq 6$ km, respectively. All heights are given above mean sea level. The temperatures T_m and T_h corresponding to 2 km and 6 km, respectively, are taken from the soundings. The two-dimensional histograms are divided into four primary sections defined schematically in Fig. 2. The nominally clear layer corresponds to pixels having $T \geq T_{cs} - 3$ K and $D \leq D_t$, where D_t is the VIS threshold count defined by Minnis et al. (1987). All other sections are considered to be cloudy. The boundary between the low and middle clouds is given by the line designated P_m, which represents the solution of (8) for $T_c = T_m$. High and mid-level clouds are separated by P_h, where T_ϵ is computed for $T_c = T_h$. The quantities computed for each layer are denoted with the subscripts; 1, 2, 3, or 4 for clear, low, middle, or high, respectively.

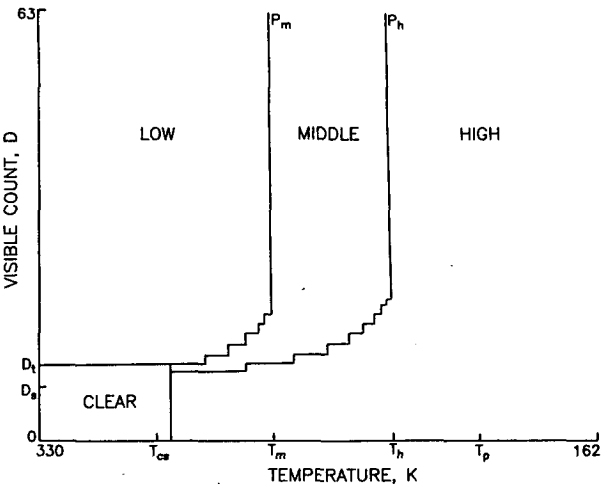

FIG. 2. Schematic bispectral histogram illustrating boundaries for clear and cloud-layer classifications.

2) LAYER CLOUD PARAMETERS

For the kth layer, the areal fraction is

$$C_k = N_k/N_t,$$

where

$$N_k = \sum_{ij} n(T_i, D_j),$$

n is the number of pixels having T_i and D_j, the limits i and j are defined only for layer k, and N_t is the total number of pixels in the histogram. The temperatures in a given cloud layer are averaged for each VIS count. Thus, for D_j

$$T_{kj} = B^{-1}[\sum_i B(T_i)n(T_i, D_j)/N_{kj}],$$

where

$$N_{kj} = \sum_i n(T_i, D_j).$$

Given $\epsilon_j = \epsilon(D_j)$, the average cloud-center temperature for layer k is

$$T_k = B^{-1}\left\{\frac{\sum_j N_{kj}[B(T_j) - (1 - \epsilon_j)B(T_{cs})]/\epsilon_j}{N_k}\right\}.$$

If $T_k < T_p$, $T_k = T_p + 1$ K, where T_p is the tropopause temperature taken from the soundings. The emittance is adjusted accordingly. The layer temperatures are then adjusted as in Minnis et al. (1987) to account for cloud contamination of the clear-sky temperature. The mean cloud-top temperature of the layer, T_{tk}, is found from (6) and (7) using $T = T_j$ and $T_c = T_k$.

In the analysis performed by MYSAG, cold, obviously cloudy pixels were observed, which were visibly too dim to analyze with (1). These "dark" pixels are left out of the initial processing. It is assumed that the

dark pixels are high clouds at the same height as the average found for the visibly detectable high-cloud pixels. Thus, an emittance is computed for each dark pixel based on its temperature and T_4. If $T_4 = 0$ (i.e., no nondark pixels), then $T_4 = T_p - 2$ K. This option, which assumes that the clouds in the dark pixels are high and thin, is based on the trend of decreasing emittance with decreasing cloud temperature (e.g., Platt et al. 1987).

Average VIS optical depth, τ_{v_k}, is computed for each layer and used with T_{c_k} to determine the mean thickness, h_k, of the clouds in the layer. Similarly, layer cloud emittance, ϵ_k, is also computed from the observed emittances. The layers are combined to obtain total cloud amount,

$$C = C_2 + C_3 + C_4;$$

mean cloud-center temperature,

$$T_c = B^{-1}\{\sum_{k=2}^{4} B(T_k)C_k/C\};$$

mean cloud-top temperature,

$$T_t = B^{-1}\{\sum_{k=2}^{4} B(T_{t_k})C_k/C\};$$

mean cloud thickness, h; VIS optical depth, τ_v; and emittance, ϵ. Cloud center and top heights are also determined from the mean and layer cloud temperatures.

c. Uncertainties

MYSAG analyzed coincident GOES and lidar data taken over Ft. McCoy (FMC), Madison, and Wausau (WAU), Wisconsin, to derive mean cloud-center and -top heights and cloud thicknesses, optical depths, and emittances for each half-hour during the case study period. Their results, employed to derive some of the relationships used in this study, comprise a "truth" set for estimating the uncertainties in the present analyses. The GOES data used in the MYSAG study were analyzed here with the methodology outlined in the previous section. Averages of the differences between the resulting satellite-derived parameters and those determined using both lidars and satellites by MYSAG (the truth set) are assumed to represent reasonable estimates of the uncertainties in the parameters derived for the entire IFO region. It is implicit that the clouds over the three lidar sites are typical of the entire region.

Figure 3 shows a comparison of the various parameter values computed for FMC during the 28th using the approach outlined for this study compared to those derived by MYSAG for the same data. The satellite-derived cloud emittances (Fig. 3a) are generally within ±10% of the lidar results with the greatest differences occurring near 1700 UTC and 2200 UTC. At 1700 UTC, the large emittance error converts to a difference

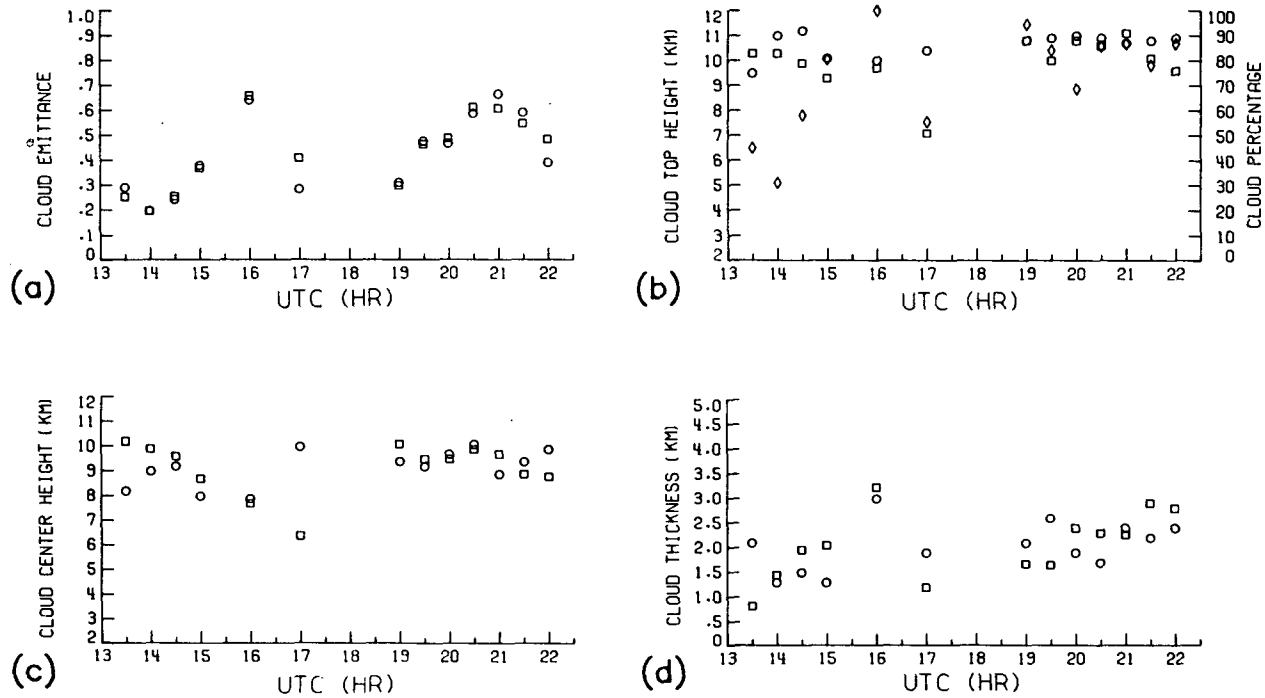

FIG. 3. Comparison of satellite-derived (squares) and lidar- and satellite-derived (circles) cloud parameters over FMC during 28 October 1986. Diamonds indicate satellite-derived cloud percentage.

of nearly 3 km in z_c (Fig. 3b), although the corresponding error in z_t (Fig. 3c) is only half of that value. Much of this error is due to the presence of a midlevel cloud as discussed below. Cloud thickness (Fig. 3d) is generally within ±1 km, except for 1330 UTC. The VIS optical depths are not plotted here. They were within ±0.1 of the reference FMC values.

Table 2 summarizes the average bias and rms differences between the satellite results and the truth set 28 October over all three sites. The 1700 UTC data over FMC were not used in the statistics due to the lidar-observed cloud deck near 4.3 km. This lower cloud was detected by the satellite and lidar analyses but was not used in determining z_c from the lidar data. The magnitudes of the rms and bias errors in h and τ_v are primarily due to the data taken over Madison. At that site, the mean value of h was derived simply from the difference between the average base and top altitudes without regard to space between sublayers. Over the other two sites, only those altitudes containing some significant lidar backscatter intensity were included in the determination of cloud thickness eliminating some of the clear space between sublayers. Given that several distinct sublayers were common during the case study period (Starr and Wylie 1990), the actual physical thickness of the clouds over Madison was probably less than that obtained using a simple difference in cloud top and base altitudes. Thus, the uncertainties in retrieved cloud thickness may be smaller than those given in Table 2.

Given the uncertainties in z_c, ϵ, and τ_v for the truth set (MYSAG) and the number of samples, it is concluded that the bias errors in those quantities are statistically insignificant for total cloud cover. The biases in z_t require some additional explanation.

Figures 4a and 4b show comparisons of z_{t3} and z_{t4}, respectively, with the lidar results for all three sites. Retrieved values of C_3 and C_4 are also included in these figures. As shown in Table 2, the average bias in cloud-top height is reduced from approximately 0.5 km to approximately −0.1 km if only high clouds are considered. Similarly, the rms error is reduced from ~0.9 to ~0.6 if only high clouds are compared with the lidar results.

TABLE 2. Differences between cloud parameter values derived with lidar-satellite dataset and satellite data only.

Difference (Lidar − Satellite)	Bias	rms
Total cloud		
z_c (km)	−0.18	0.94
z_t (km)	0.53	1.90
h (km)	0.29	1.00
ϵ (%)	−2.4	12.9
τ_v (%)	−12.2	38.8
High clouds only		
z_c (km)	−0.41	1.13
z_t (km)	−0.09	0.63

The percentage of retrieved midlevel clouds is small in most cases. Some of the midlevel clouds may actually be due to pixels which are only partially filled with a high cloud. Others, such as those observed near 6 km, may be the fall streaks of higher clouds reaching altitudes just below the high cloud threshold. Scattered stratocumulus clouds were observed during the day over some sites at $z \approx 4$ km (Starr and Wylie 1990). Thus, many of the clouds retrieved over the lidar sites between 3.6 km and 4.8 km probably correspond to stratocumulus clouds which did not happen to pass directly over the lidars and, therefore, were not evident in the lidar returns. The lidar samples an area of the sky that is only a few meters wide, while the satellite samples a 16-km-wide swath over the site.

For one case having a lidar-detected midlevel cloud, 1700 UTC over FMC, the satellite cloud-layer analysis shows a midlevel deck with $z_t \sim 5$ km (Fig. 4a) and a high-cloud deck with $z_t \sim 11$ km (Fig. 4b). The latter height is slightly greater than the maximum values of z_t observed over FMC during the half-hour centered at 1700 UTC (Sassen et al. 1990). The former altitude corresponds closely to a distinct middle-layer cloud which was detected by the FMC lidar (Sassen et al. 1990). In this instance, the midlevel clouds comprised 50% of the total cloud cover. Advection of this midlevel deck behind the cirrus clearing (Starr and Wylie 1990) probably accounts for the midlevel clouds retrieved over WAU at 1800 UTC. The lidar-observed clouds at 4 km over WAU around 2030 UTC (Sassen et al. 1990), however, were probably obscured by cirrus clouds since the satellite retrievals indicate only high clouds at that time.

It is not clear from these results whether the uncertainties in the satellite analysis of total cloud heights are due primarily to sampling differences in the satellites and lidars or to partially cloud-filled pixel effects. More detailed logs of visual observations would be helpful in determining when low or midlevel clouds were in the vicinity of the lidar sites. Nonetheless, it is concluded that the bias errors are insignificant if only high clouds are considered. Based on the uncertainties in the values of z_c, z_t, and h (see MYSAG) and the rms differences in Table 2, it is concluded that the cloud-center and cloud-top heights from a given retrieval are usually within ±0.6 km of the actual values. Cloud thicknesses are expected to be within ±0.7 km of the actual cloud depths, at least when total cloud depth is considered. It should be noted that the uncertainties discussed here apply only to single-layer clouds over the IFO during the case study period. In multiple-layer cloud fields (i.e., two or more distinct cloud layers stacked vertically), the observed radiances will probably produce cloud-center altitudes somewhere between the two clouds when the upper-level cloud is optically thin. In those situations, the derived cloud-

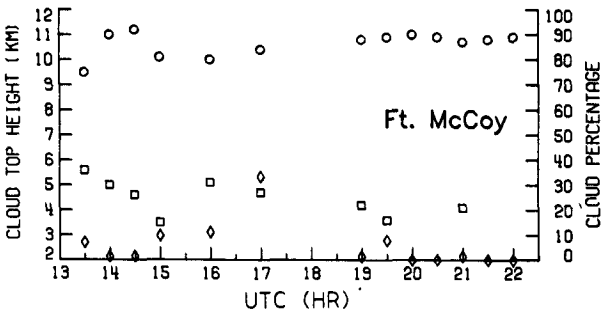

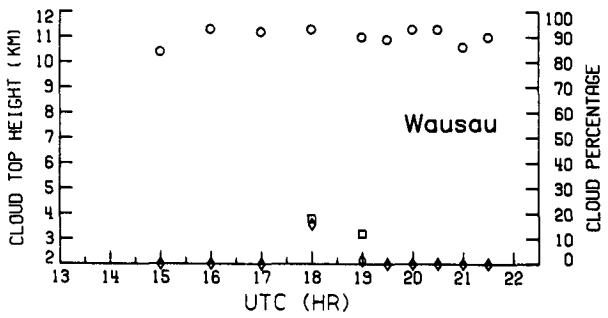

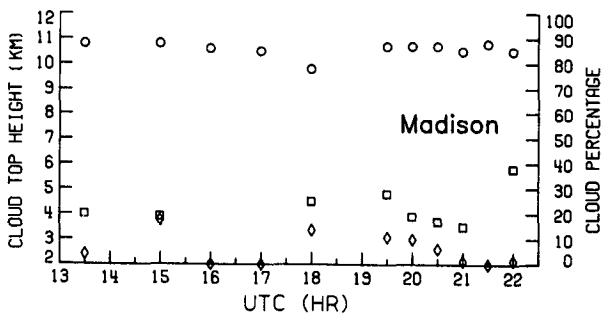

FIG. 4a. Comparison of satellite-derived midlevel cloud-top heights (squares) and lidar-derived cloud-top heights (circles) during 28 October 1986. Midlevel cloud amounts (diamonds) are also shown.

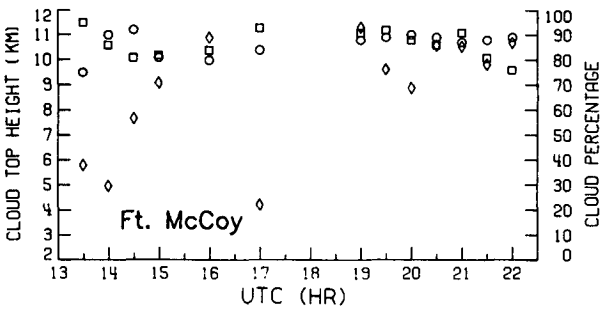

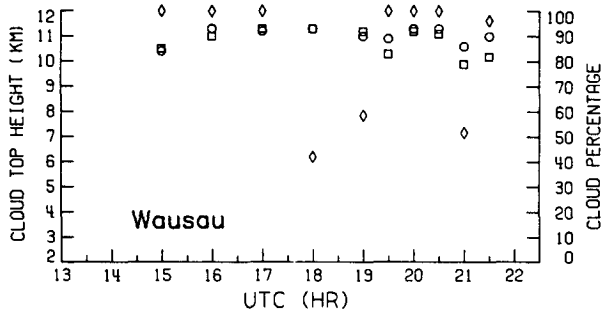

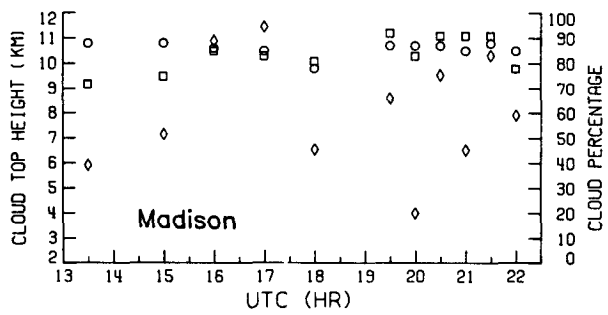

FIG. 4b. Same as Fig. 4a, except for high clouds.

top height will be less certain than for the cases examined above.

4. Results and discussion

a. Clear-sky albedos

The midday (1800 UTC), clear-sky VIS albedos for the IFO study area are plotted in Fig. 5 for 28 October. Values of α_s range from 9% over the lakes to 13% over northeastern Iowa. The IFO diamond of surface sites (Starr 1987) is denoted with the asterisks in Fig. 5. Over FMC and WAU, the western and northern asterisks, respectively, $\alpha_s \approx 10.5\%$ at noon. Figure 6 shows the variation of GOES-derived values of α_s (solid line) and ρ_s (dashed line) with UTC over WAU on the same day. Clear-sky bidirectional reflectance (dashed line) varies from a nearly constant value of 14% in the morning to ~16% during the afternoon. During the early morning and at 2200 UTC, the view from GOES is more perpendicular than parallel with the solar plane so that some of the shadowing due to surface texture is observed by the satellite. This effect results in a reflectance which is lower than the albedo. The changing sun position brings the satellite closer to the antisolar point during the remainder of the day so that the reflectance is greater than the albedo. At 1800 UTC, the view is only a few degrees from the antisolar point. This variation of ρ_s during the day is consistent with the land bidirectional reflectance model of Minnis and Harrison (1984b) for these viewing conditions. Application of χ_s in (2) removes the viewing angle dependence of ρ_s resulting in a nearly symmetrical variation of α_s about local noon. The change in α_s of ~7% from noon to the terminator is typical of most of the IFO region and of the solar-zenith-angle dependence of clear-sky albedos over land in general.

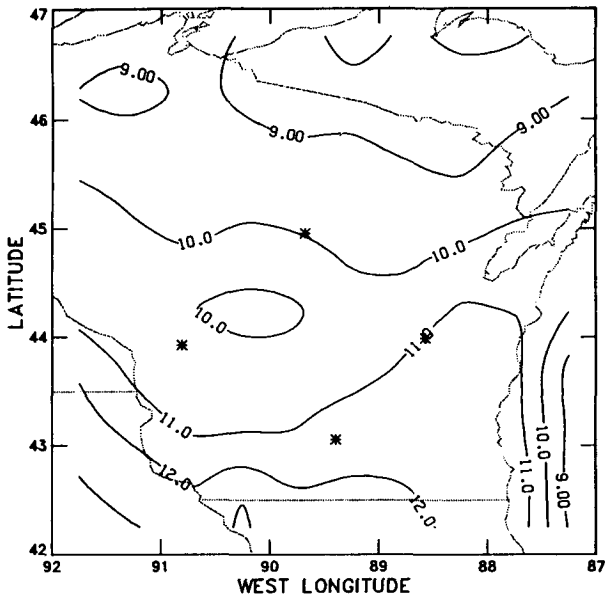

FIG. 5. Clear-sky, visible albedo in percent for 28 October 1986 at 1800 UTC.

b. 27 October cloud and radiative parameters

Variations in GOES-derived high cloud amounts, altitudes, and emittances over the IFO region are plotted in Figs. 7, 8, and 9, respectively, for 1800 UTC through 2100 UTC during 27 October 1986. As noted by Starr and Wylie (1990), an apparent mesoscale disturbance enters northwestern Wisconsin around 1800 UTC as a "wave" of significant high cloud amounts. This feature penetrates southward to ~43°N by 1930 UTC before folding to the northeast over the next two hours. The area of highest and thickest clouds ($z_{t_4} > 11$ km, $\epsilon_4 > 0.4$) travels eastward at ~46°N. The clouds near the southern tip of this wave seem to be broken and optically thin. This tip area, apparently cut off from the main disturbance by 2030 UTC, progresses more slowly to the east at ~44°N. Visible optical depths range from approximately 1.5 in the north to values less than 0.5 south of 45°N, while retrieved thicknesses range from less than 0.5 km thick near the tip and along the edges of the cloud field to 3 km near the center of the disturbance. Based on the cloud thickness and emittance variations, it appears that the cloudiness develops until ~2100 UTC as the wave begins to fold to the northeast.

The broken and tenuous nature of the clouds near the trough of this wave makes accurate retrievals more difficult than in the thicker portions. For example, over FMC, the high cloud fraction varies from 17% at 1930 UTC to 44% at 2100 UTC. At 1930 UTC, $z_{t_4} \approx 12$ km and $\epsilon_4 \approx 0.1$. Significant midlevel cloudiness (28%) ($z_{t_3} \approx 7$ km) was also identified at this time although there was no indication of their presence from other observations, i.e., lidar or surface observers. The resulting mean cloud-top height, ~8.5 km, probably underestimates the true cloud height by 1 km.

At 2030 and 2100 UTC, few midlevel clouds were detected over FMC. The high cloud top altitudes, 9.1 km and 9.4 km, are similar to those observed with the FMC lidar (Sassen et al. 1990). The lidar at WAU observed scattered subvisual clouds between 1800 and 2100 UTC. No clouds were detected with the satellite over WAU until 2030 UTC (2000 UTC data are missing). The radiative effects of the subvisual layer at 11.2 km combined with a thicker layer at ~8.6 km (Sassen et al. 1990) are detected with the satellite analysis which yields z_{t_4} = 10.0 km and 9.3 km at 2030 UTC and 2100 UTC, respectively, over the WAU vicinity. The extremely low emittance ($\epsilon < 0.07$) of the subvisual clouds apparently causes less than a 3 K change in the observed 11.5-μm temperature, so the cirrus are undetected.

The characteristics of the main cloud field as observed by the GOES are in good agreement with the lidar observations taken by the ER-2 (Sassen et al. 1990). Cloud-top heights from the ER-2 at ~46°N at ~1900 UTC show a decrease from 11.2 km at the center of the cloud mass to 10.5 km away from the center. Cloud thickness estimated from the ER-2 plots is ~2.5 km in that area. The lidar heights range from 9.2 to 10.3 km at 45°N at 1930 UTC. Around 2030 UTC between WAU and FMC, the lidar cloud-tops vary from 8.9 to 10.0 km compared to 9.1 to 10.0 km from the GOES. Thus, except for the very thinnest cloud fields, the GOES analysis yields a relatively accurate picture of the vertical and horizontal variations in the cirrus cloud fields over the IFO region during the daytime on the 27th.

The consistency of this retrieval approach may be evaluated by comparing the values for each parameter derived from GOES data taken at 1930 UTC to those derived from the near-simultaneous AVHRR data. Images of the greater IFO area taken from the GOES and AVHRR data at 1930 UTC on the 27th are shown in Fig. 10. All of these images have been projected onto rectangular latitude–longitude grids of 0.02° for 1-km

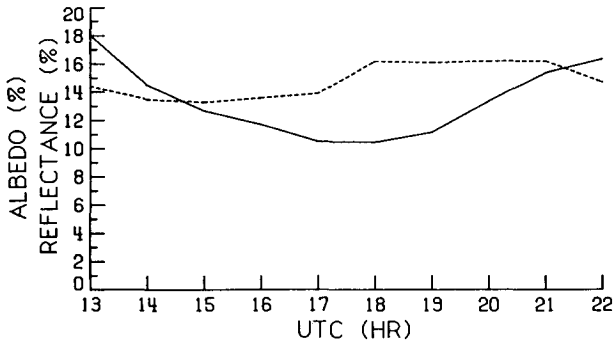

FIG. 6. Clear-sky, visible albedo (solid) and bidirectional reflectance (dashed) over WAU, 28 October 1986.

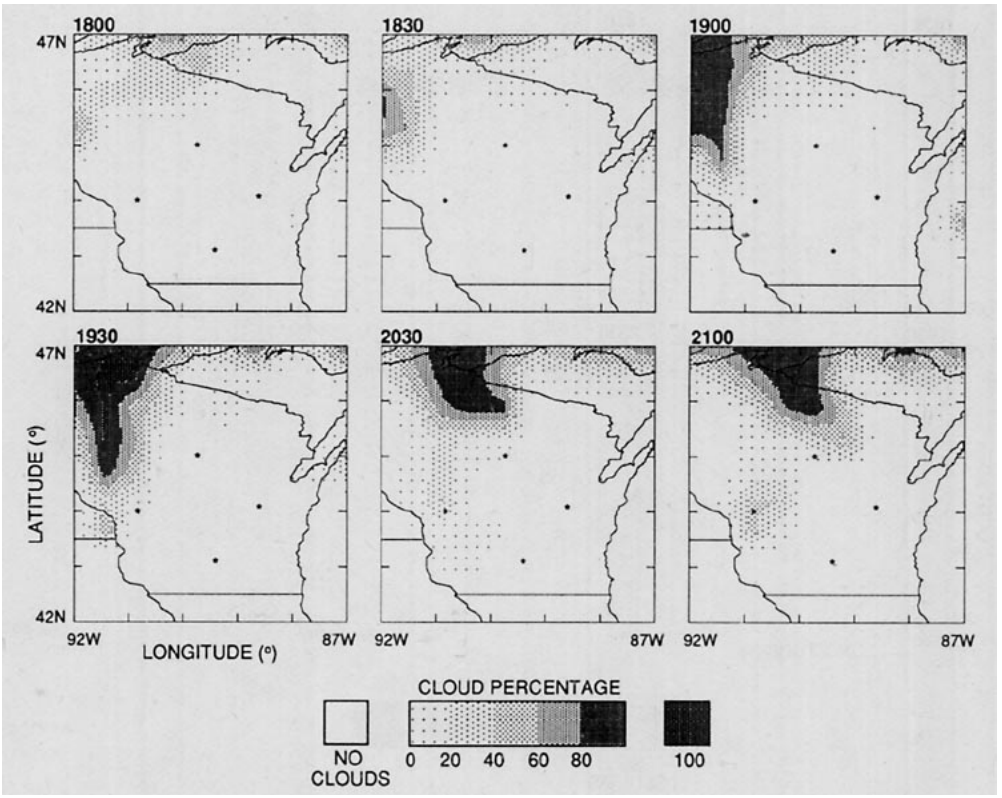

FIG. 7. GOES-derived high cloud amounts during 27 October 1986. Times (UTC) shown in bold.

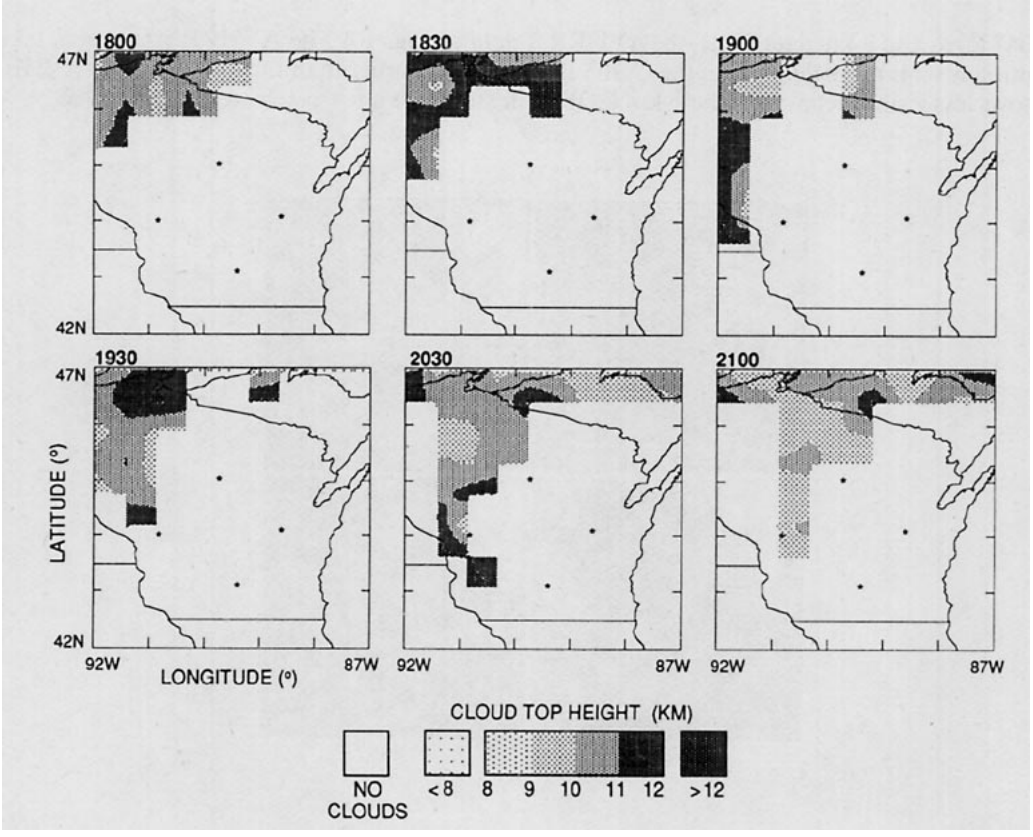

FIG. 8. Same as Fig. 7, except for high cloud-top height in km MSL.

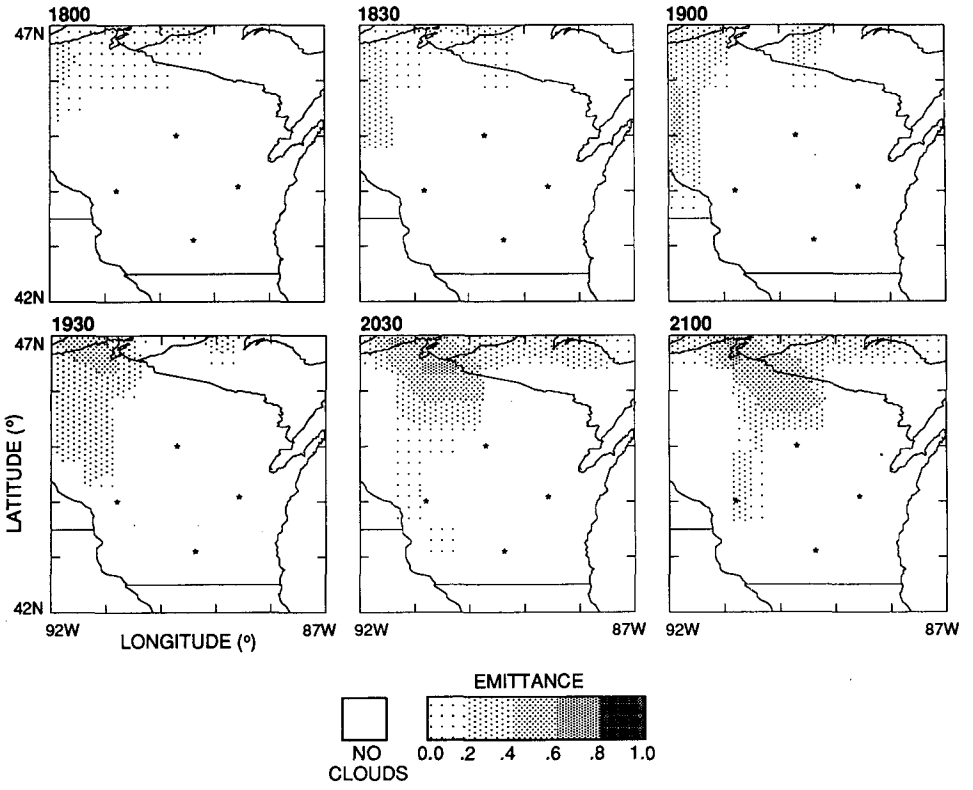

FIG. 9. GOES-derived high-cloud emittance during 27 October 1986. Times (UTC) shown in bold.

data and 0.04° for 4- and 8-km data. Note, the AVHRR 4-km resolution reveals more detail than the GOES IR data, but shows less visible detail than the 1-km GOES data in Fig. 10. The AVHRR image was taken a few minutes earlier than the GOES, so the AVHRR cloud features are a few pixels west of the GOES. A westward

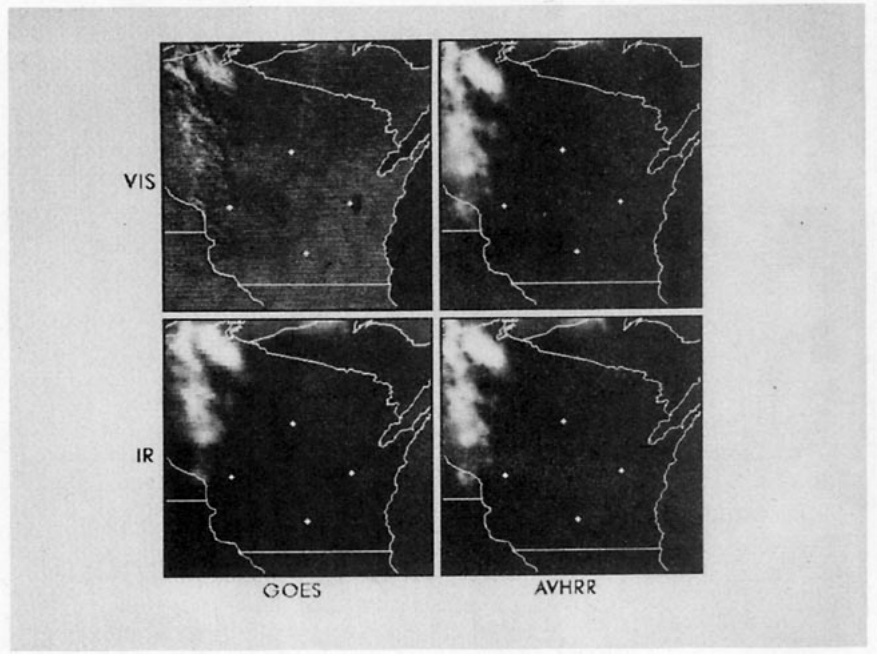

FIG. 10. Satellite imagery over the IFO region at 1930 UTC 27 October 1986.

shift of ~0.1°, required to correctly navigate the GOES data in the pictures, was not applied to the analyzed data. Therefore, the analyzed GOES results will appear further to the east than the AVHRR parameters.

Some of the reflectance and temperature discrepancies in the photographs are due to navigation, time, calibration, and resolution mismatches. The main causes of the differences, though, are due to viewing angle effects. On both the 27th and 28th, the GOES viewing zenith angle was ~53° at the center of the area. At 1930 UTC, the relative azimuth angle of the GOES was ~161°. During the 27th, $\psi \sim 39°$ and $\theta \sim 51°$ for the AVHRR. Thus, the satellites viewed the region from nearly opposite directions relative to the sun. Over land, there are an antisolar maximum and a forward-scattering minimum near $\theta = 30°$ in the bidirectional reflectance patterns due to surface texture effects. A forward scattering maximum is observed for both cloud and water bidirectional reflectances (Minnis and Harrison 1984b). Thus, the land and water are distinct in the GOES VIS image but not in the AVHRR picture. For example, Lake Winnebago near the right apex of the IFO diamond does not appear in the AVHRR image. The anisotropic reflectance differences also reduce the cloud–land contrast in the GOES visible data but enhance it for the AVHRR. The thin clouds in the center-left part of the region are very faint in the GOES VIS image but are quite evident in the AVHRR data. There is more similarity in the IR images since the viewing angle has a relatively small effect on the IR radiance.

Since the AVHRR had such different viewing conditions, it was necessary to adjust χ_c derived from the GOES angles to the AVHRR angles. A new anisotropic reflectance factor was found by adjusting χ_c to obtain a match in the cloud heights at the center of the wave. This adjustment resulted in $\chi_c(\text{AVHRR}) = 1.5$. The ratio of $\chi_c(\text{AVHRR})/\chi_c(\text{GOES}) \sim 1.2$, is 20% greater than expected from the cloud bidirectional reflectance model of Minnis and Harrison (1984b). This greater anisotropy in the data is more likely due to the larger optical depth of the average cloud in the empirical cloud reflectance model. Increasing optical depth tends to diminish the anisotropy.

Although there is only one data point for comparison here, the multiangle views permit a check on the model used in the methodology. Calculations for the same angles were performed for $\tau_v = 1$ using the adding-doubling model of Takano and Liou (1989b) with the scattering phase functions for randomly oriented hexagonal crystals (Takano and Liou 1989a) having the same dimensions as those used in the albedo model and for water droplets with an equivalent radius of 10 μm. It was found that the ratio of the theoretical ice-crystal reflectances was ~1.5 compared to ~3.0 for the water-droplet reflectances. Thus, the required adjustment in χ_c is much closer to that expected from theory for a cloud containing randomly oriented hexagonal ice columns than to the value expected for a water droplet cloud. The consistency between the observations, reflectance parameterization, and theory lends additional support to the approach taken here to interpret the radiances over the cirrus fields.

In general, the AVHRR results in Fig. 11 are in good agreement with the GOES parameter values considering the time and navigation differences. Some additional cloud cover is detected with AVHRR data just north of WAU. The AVHRR cloud emittances also tend to be slightly higher and the cloud-center heights slightly lower than those derived from the GOES data.

The clear-sky broadband albedos from ERBE (Fig. 12) are between 15% and 20%, while the clear-sky longwave flux is ~270 W m^{-2}. Cirrus clouds increase the albedo by ~9% near the Wisconsin–Minnesota border. At $\theta = 60°$, this albedo change translates to an energy loss of ~50 W m^{-2} for the surface-troposphere system balancing the corresponding decreases in M_{lw}, which are as large as 50 W m^{-2}. Thinning and lowering of the cirrus towards the south are revealed in Fig. 12 as contours of decreasing albedo and increasing longwave flux.

c. 28 October cloud and radiative parameters

Cloud conditions during the following day were more complicated. Figure 13 shows the GOES imagery of the IFO region during the morning. It is difficult to follow a given feature because the clouds are developing and dissipating at different levels as the system progresses across the region. At 1400 UTC, there is an apparently brighter and higher cloud field in the northwest compared to more broken, lower clouds over the remainder of Wisconsin. Examination of the cloud shadows indicates the cloud-top heights range from about 7.8 to about 8.4 km in the southern part of the state. The higher cloud field appears to move over central Wisconsin by 1600 UTC, followed by a wedge-shaped mass of clouds to the northwest. Analysis of the shadows in southern Wisconsin indicates that the cloud tops vary between 8 and 9 km. A hint of clearing is evident in the southwestern corner of the region. By 1800 UTC, the "wedge-shaped" cirrus (see Starr and Wylie 1990) has become more organized. The clearing line behind the wedge moved almost halfway across the region in two hours. A line of bright, midlevel clouds lay between FMC and WAU with a more tenuous cirrus field to the west. Thick midlevel clouds have also pushed into northwestern Wisconsin.

The development and progression of these cloud fields are quantified in the time series of the various parameters (Figs. 14–22). Hourly values of total cloud amount, total cloud-top altitude, and total cloud VIS optical depth are contoured in Figs. 14, 15, and 16, respectively. High cloud amounts and values for z_{t_4} are plotted in Figs. 17 and 18, respectively. Figures 19, 20, 21, and 22 depict the 3-hourly variations in total cloud

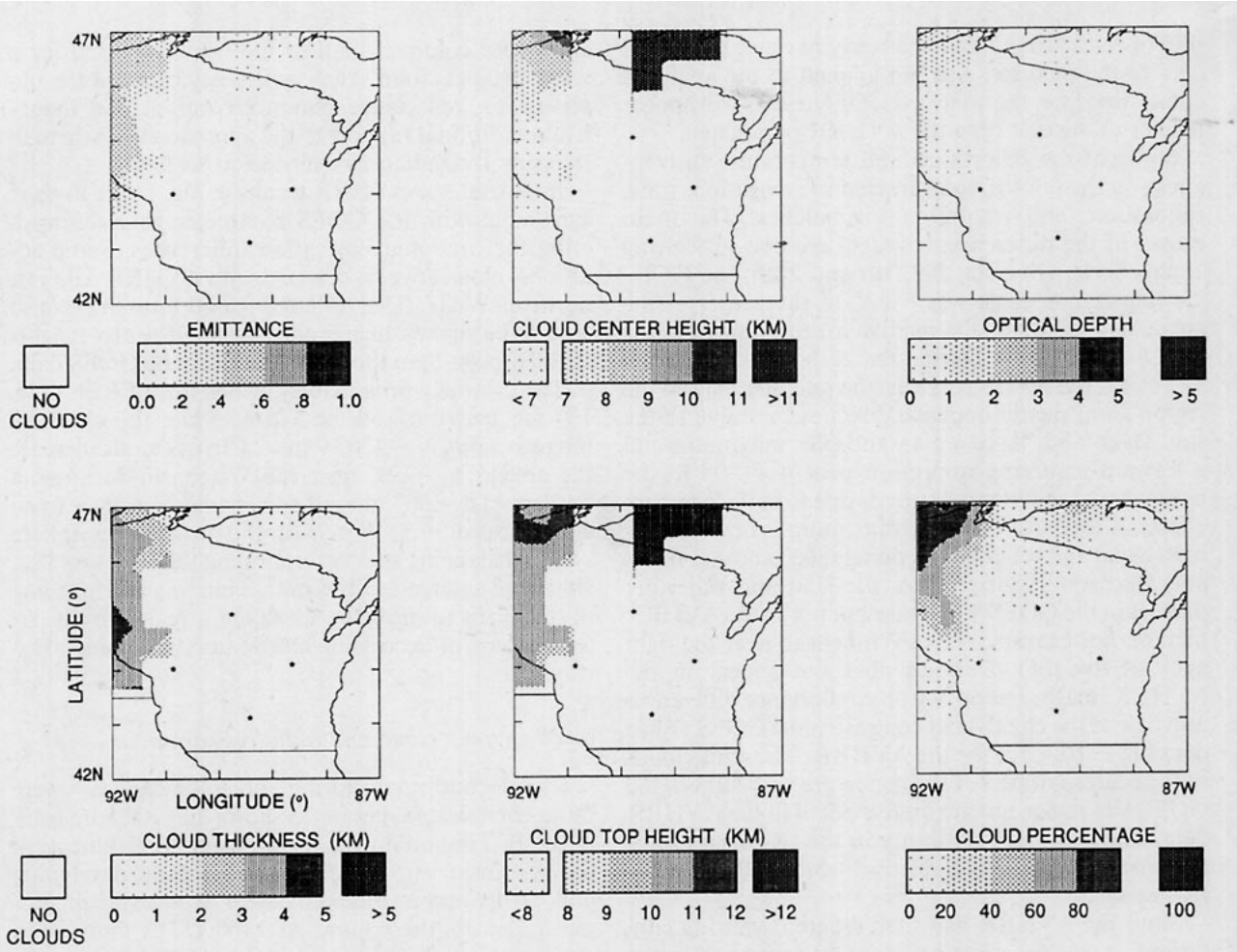

FIG. 11. AVHRR-derived high-cloud parameters at 1930 UTC 27 October 1986.

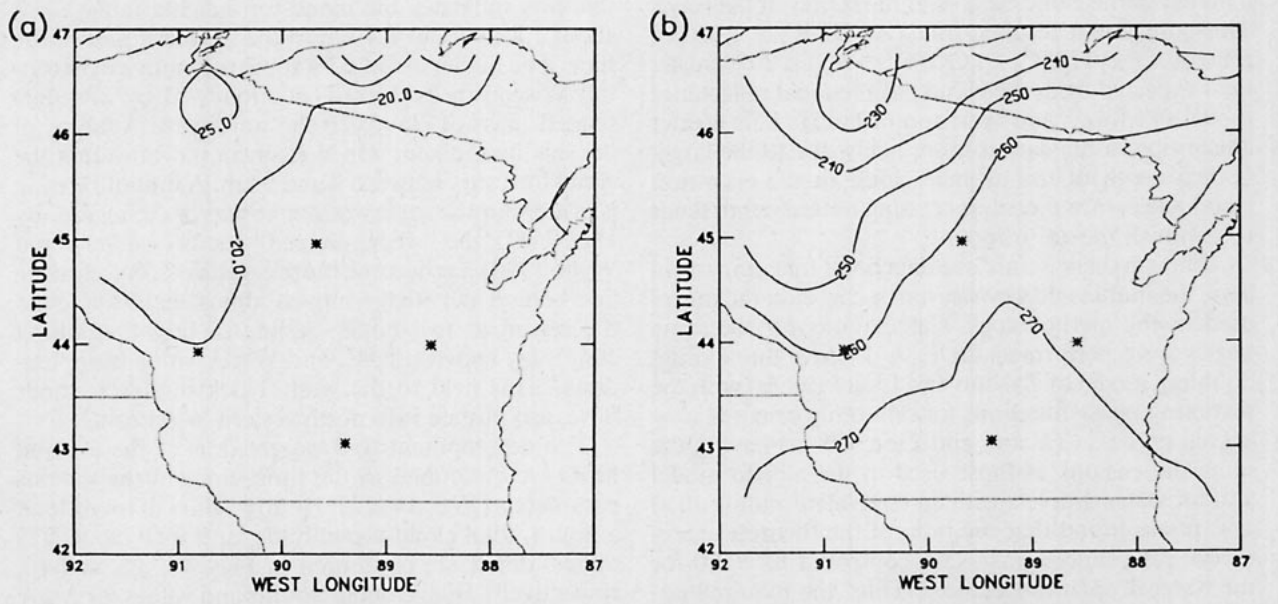

FIG. 12. Broadband radiation components at the top of the atmosphere from the ERBE at 1930 UTC 27 October 1986 (a) albedo, in percent; (b) longwave flux in W m^{-2}.

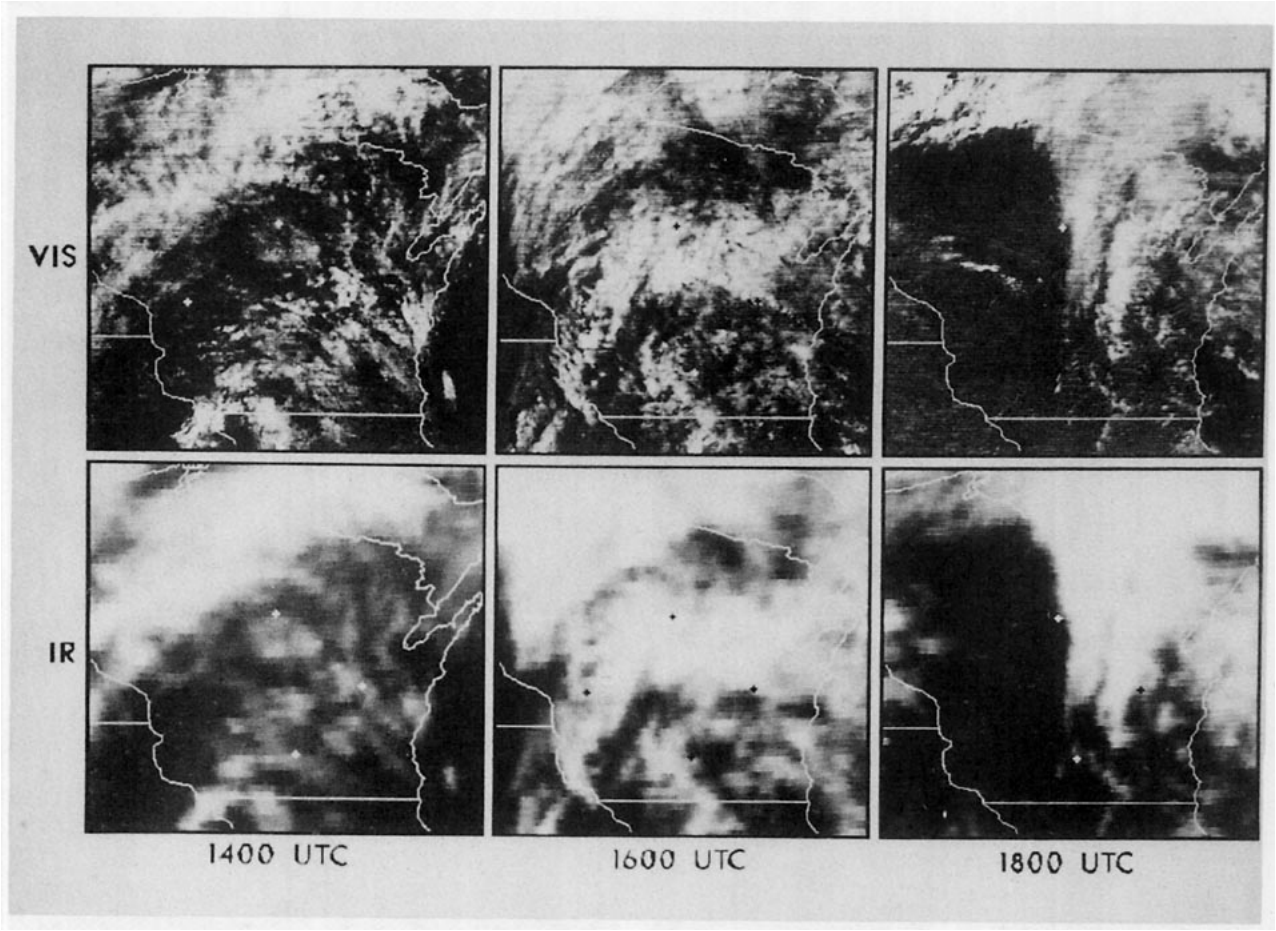

FIG. 13. GOES imagery taken over the IFO region during 28 October 1986.

emittance, thickness, cloud-center heights, and midlevel cloud amounts, respectively.

Except for the clear tongue, which passed through the region during the afternoon (Fig. 14), the total cloud cover was generally greater than 80% over the region. Most of the cloudiness appears to be high clouds (Fig. 17). It should be noted, however, that midlevel clouds cannot be detected from satellites when there are high clouds above them. In the early morning, midlevel cloud amounts ranged between 20% and 40% over the eastern half of the state resulting in mean cloud-top altitudes between 7 and 8 km (Fig. 15). By 1500 UTC, most of the midlevel clouds (Fig. 22) had either dissipated, been obscured, or advected eastward so that $z_t > 8$ km over most of the region. As the high-level clouds developed in the northern half of the state, an area of apparent sinking motion, suggested by decreased cloud amounts and heights, developed near Lake Superior between 1500 and 1700 UTC. This development appears to have culminated in the mesoscale wedge cloud (Fig. 13) covering the northeastern quadrant of the region at 1800 UTC. The optical depth of this cloud system ranged from 1 to 2.5 (Fig. 16) while the average cloud-top height was greater than 11 km. On average, the cloud field was estimated to be between 2.0 and 2.5 km thick at 1800 UTC (Fig. 20). Data from Sassen et al. (1990) indicate that the cloud deck was ~4 km thick over WAU before the clearing line passed. The lidar at FMC, however, showed the cloud base rising with a decrease in cloud thickness to ~1.5 km before the clearing at 1700 UTC. Such discrepancies are probably due to horizontal variations in the cloud properties. For example, the brightest (thickest) part of the wedge appears to have passed over WAU at 1800 UTC (Fig. 13), so that the clouds passing over WAU at that time may not be particularly representative of the entire preclearing cirrus. Based on the increasing values of τ_v at 1900 and 2000 UTC, the wedge cloud continued developing as it exited the region.

The next system of cirrus clouds following the clearing and its embedded midlevel clouds (Fig. 22) was generally thinner ($h \sim 2.5$ km) than the cirrus in the morning ($h \sim 3.5$ km, see Fig. 20). The cirrus cloud-top heights remained above 10 km (Fig. 18) throughout the afternoon in the southern part of the region while an optically thick, midlevel deck entered from west-northwest. Cloud-center heights generally decreased from north to south at 1500 UTC while the reverse

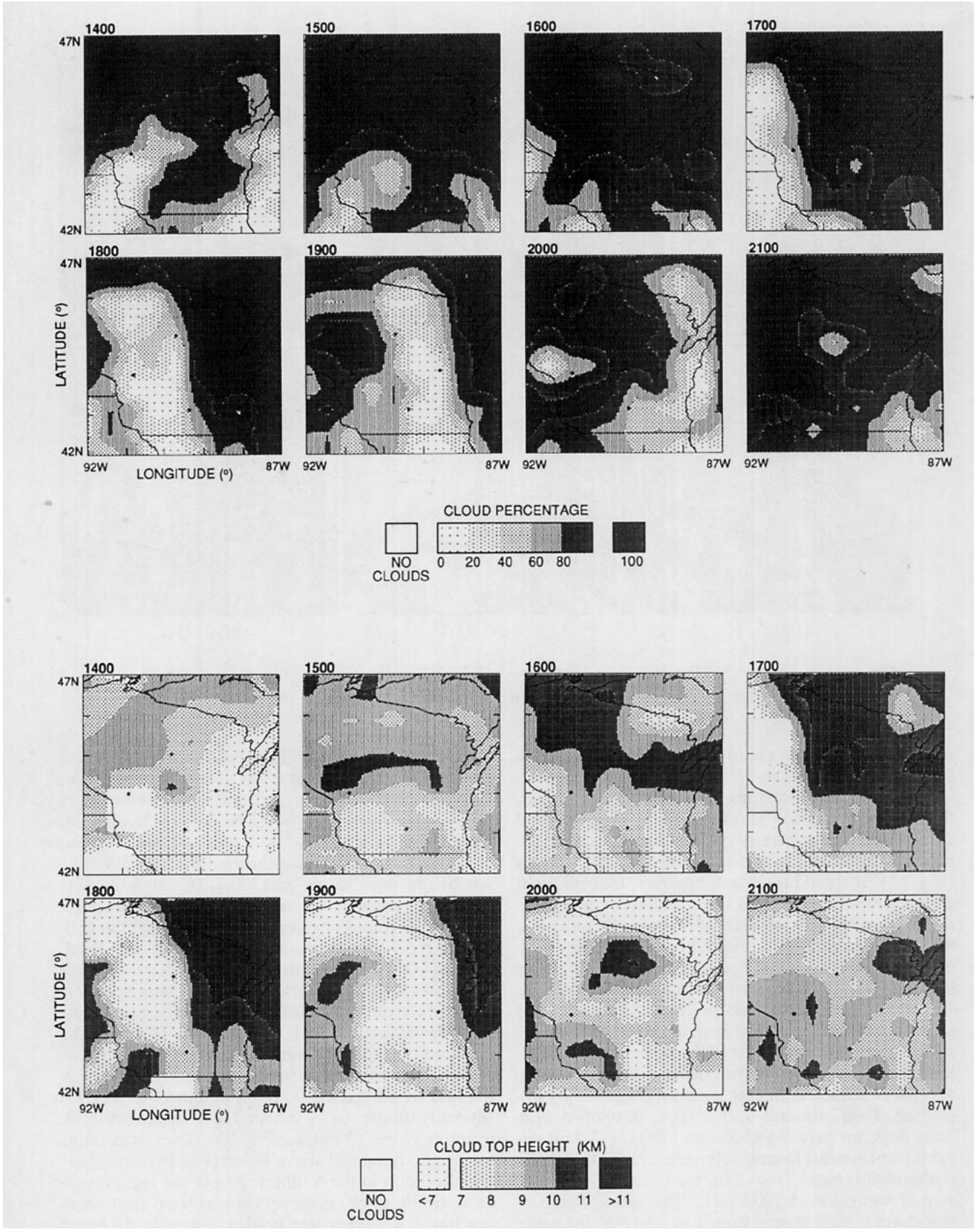

FIG. 15. GOES-derived total cloud-top altitude for 28 October 1986. Times (UTC) shown in bold.

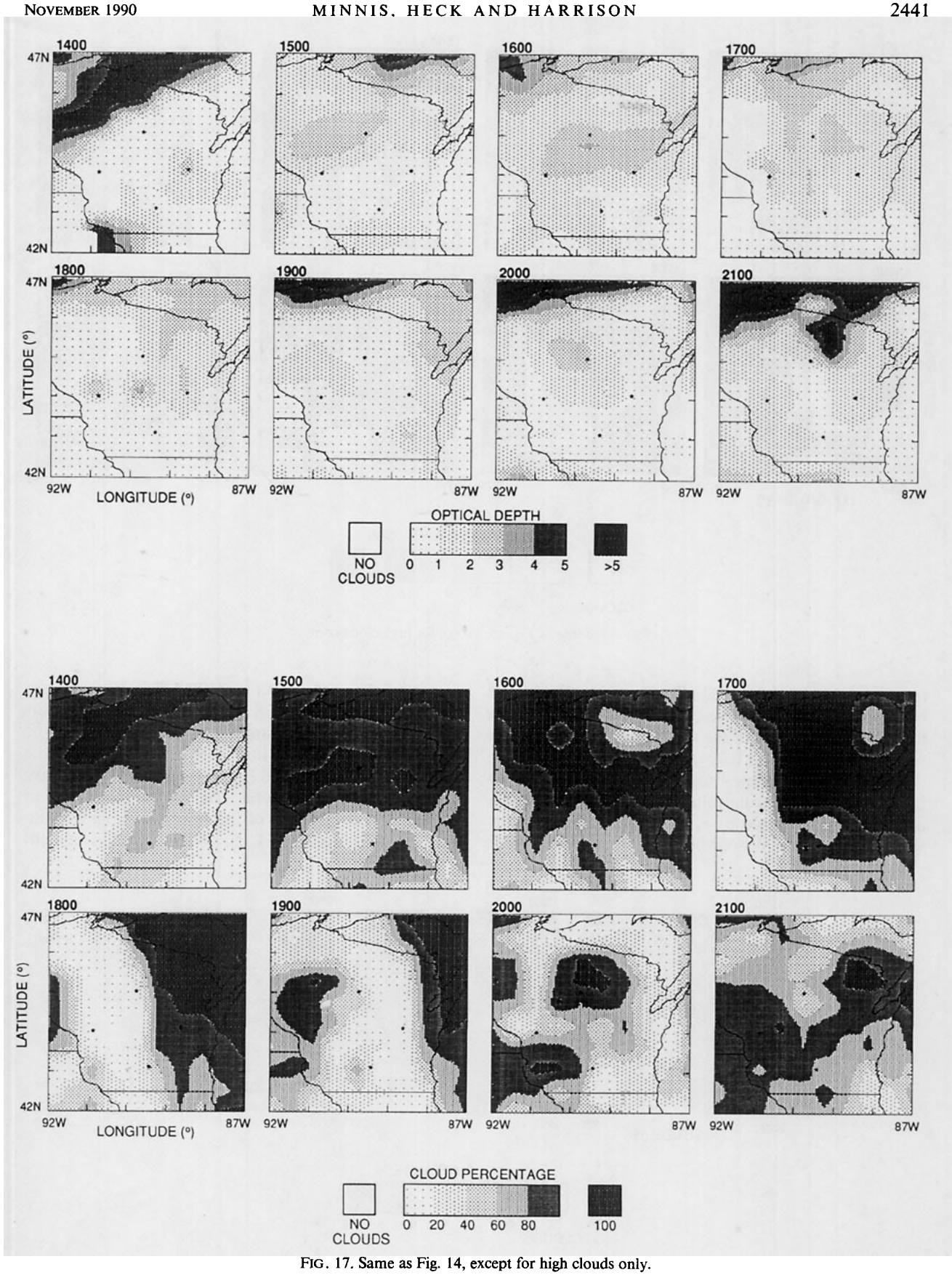

FIG. 17. Same as Fig. 14, except for high clouds only.

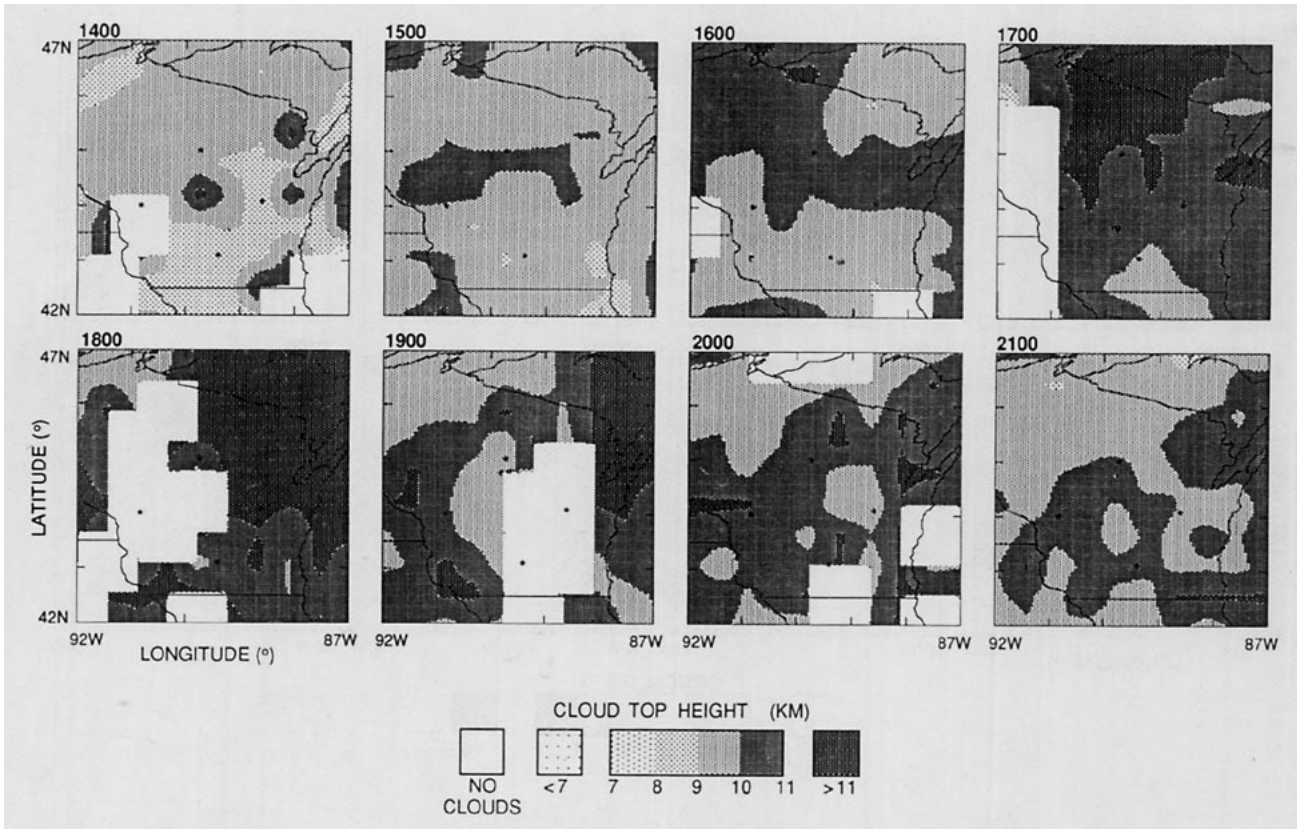

FIG. 18. Same as Fig. 15, except for high clouds only.

trend occurred by 2100 UTC (Fig. 21). The cloud beam emittance was between 0.7 and 1.0 in the north for the entire day. Over the remainder of the region, ϵ varied from ~0.15 to 0.7.

Some evidence of mesoscale cloud organization appears in the postclearing values of optical depth. A secondary wave, outlined by $\tau_v > 2.0$, seems to have developed in central Wisconsin by 2000 UTC. Satellite images of the IFO region at 2100 UTC are shown in Fig. 23 for both the GOES and AVHRR views. Results for the high cloud parameters derived from the AVHRR data are given in Fig. 24. Examination of the photographs, Fig. 24, and Fig. 17 suggests that the wave is an artifact of the analysis. The relative maximum in τ_v is about 60 km west of the maximum high cloud-top altitude (Fig. 17). This cloud feature is evident

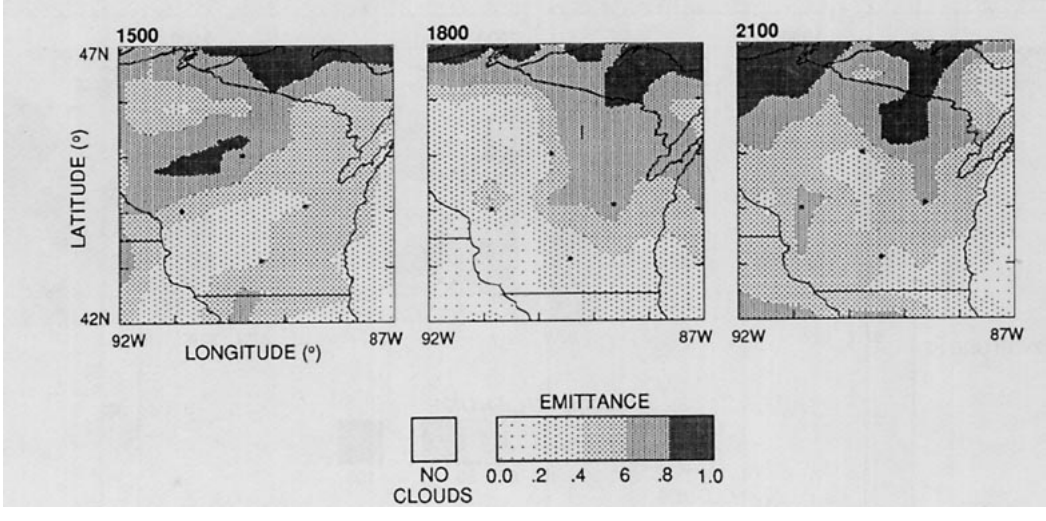

FIG. 19. GOES-derived total cloud emittance for 28 October 1986. Times (UTC) shown in bold.

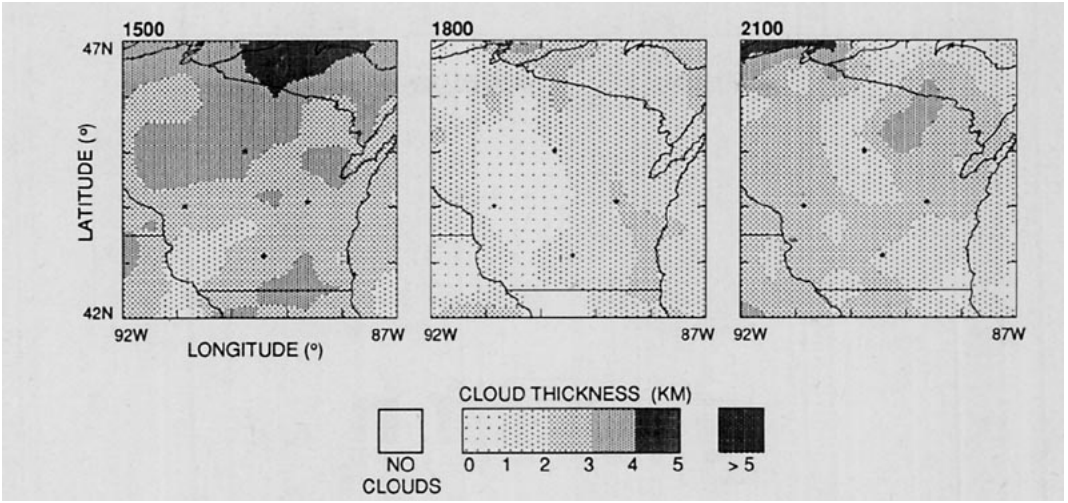

FIG. 20. GOES-derived total cloud thickness for 28 October 1986. Times (UTC) shown in bold.

over southeastern Minnesota at 1800 UTC (for better spatial coverage see the GOES IR image in the report by Starr and Wylie 1990), but it is less intense. Its development can be traced with Figs. 15 and 16. The shading for $z_t > 10$ km encompasses this cloud field northwest of FMC at 1800 UTC. The area within this contour level increased from 1800 through 2000 UTC when its southern perimeter passed over WAU. Maximum values of τ_v lay almost perpendicular to the longitudinal axis of the cloud height field. At 1900 UTC, the centers of the two fields almost coincide before separating by 2100 UTC. This particular cloud feature probably results from a developing upper level convective complex. Wind speeds above 10 km are about double those at 5 km according to the Green Bay sounding at 2100 UTC (Starr and Wylie 1990). The relative locations of the cloud heights and τ_v maxima suggest that intensification of the cloud field occurs at lower levels ($\sim$8 km) well behind the front edge of the higher cirrus (>10 km). Given the wind speeds, it is possible that precipitation from the upper level cloud is seeding the lower cloud, giving rise to its development. A more definitive explanation of its intensification would require additional study.

At 2100 UTC, $\psi \sim 147°$ for the GOES. Values for θ and ψ for the AVHRR during the 28th were $\sim$44° and $\sim$147°, respectively. Thus, the two satellites viewed the area from approximately the same direction during the 28th. The AVHRR, however, was situated 33° north of the solar plane on the 28th, while GOES was 33° south of the solar plane leading to slightly different observed cloud-shading conditions for the two satellites. Despite those differences, the retrieved cloud parameters are in good agreement.

The ERBE-derived broadband radiation parameters are shown in Fig. 25. Clear areas remaining at 2100 UTC are too small to be resolved by the ERBE sensor so no clear-sky values were available for this scene.

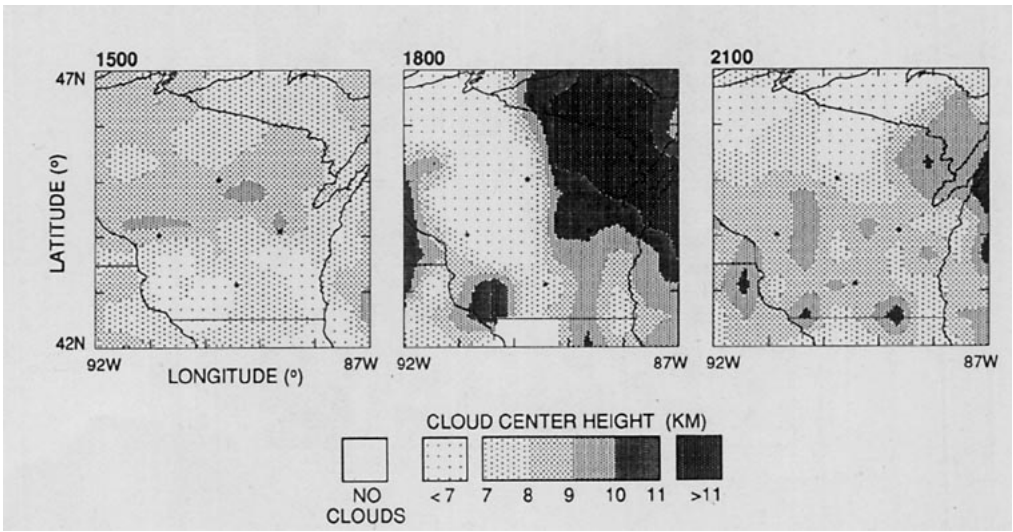

FIG. 21. GOES-derived total cloud-center height for 28 October 1986. Times (UTC) shown in bold.

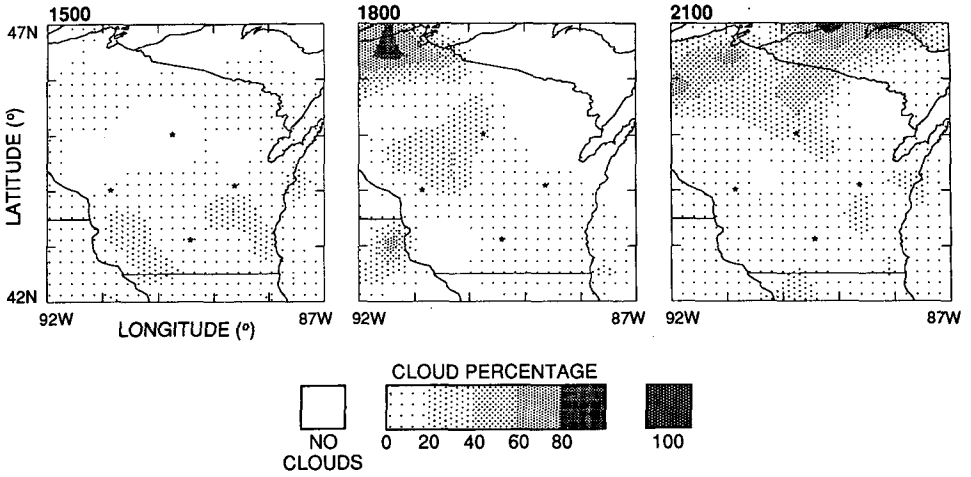

FIG. 22. Same as Fig. 14, except for midlevel clouds only.

The wave appears as a relative maximum ($\alpha > 45\%$) in the broadband albedo. Albedos greater than 70% occur in the northwestern corner of the region. The cloud feature discussed above is evident in the longwave flux minima over east-central Wisconsin. Assuming that the clear-sky longwave flux is the same as the previous day, it is estimated that the optically thin upper-level cloud is causing ~ 5 W m^{-2} warming of the cloud layer and the layers below it. The brighter cloud to the west is cooling the surface and atmosphere beneath it by ~ 15 W m^{-2}. This differential radiative heating of the atmosphere and surface may play an important role in the development of this particular cloud feature. Unfortunately, the setting sun limits further bispectral analysis of the IFO clouds.

5. Concluding remarks

A cirrus retrieval methodology similar to that used by the ISCCP was developed and tested here for the FIRE Cirrus IFO Case Study. An empirical cloud bidirectional reflectance model derived from another IFO analysis was combined with a theoretical ice crystal cloud albedo model to estimate visible cloud optical thickness, which was used to derive the cloud infrared emittance. Cloud altitude was adjusted based on the

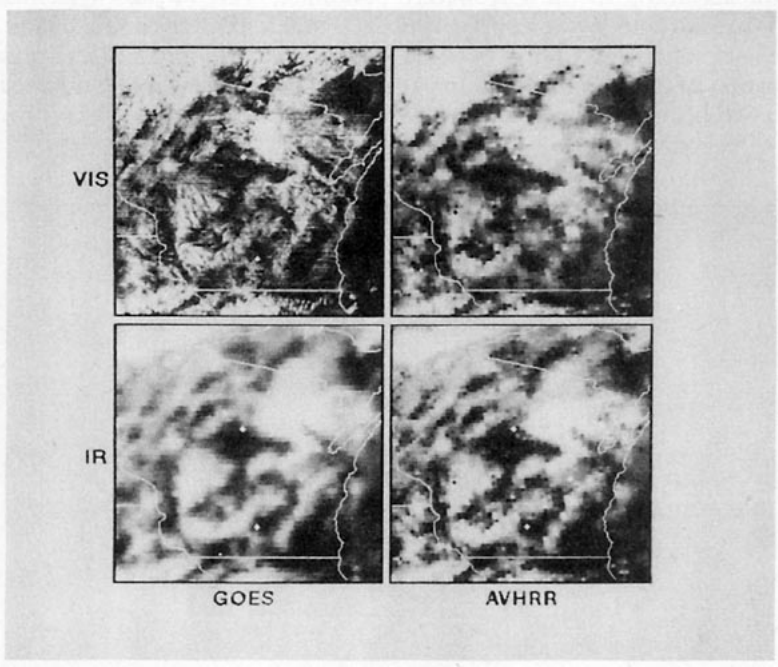

FIG. 23. Satellite imagery over the IFO region at 2100 UTC 28 October 1986.

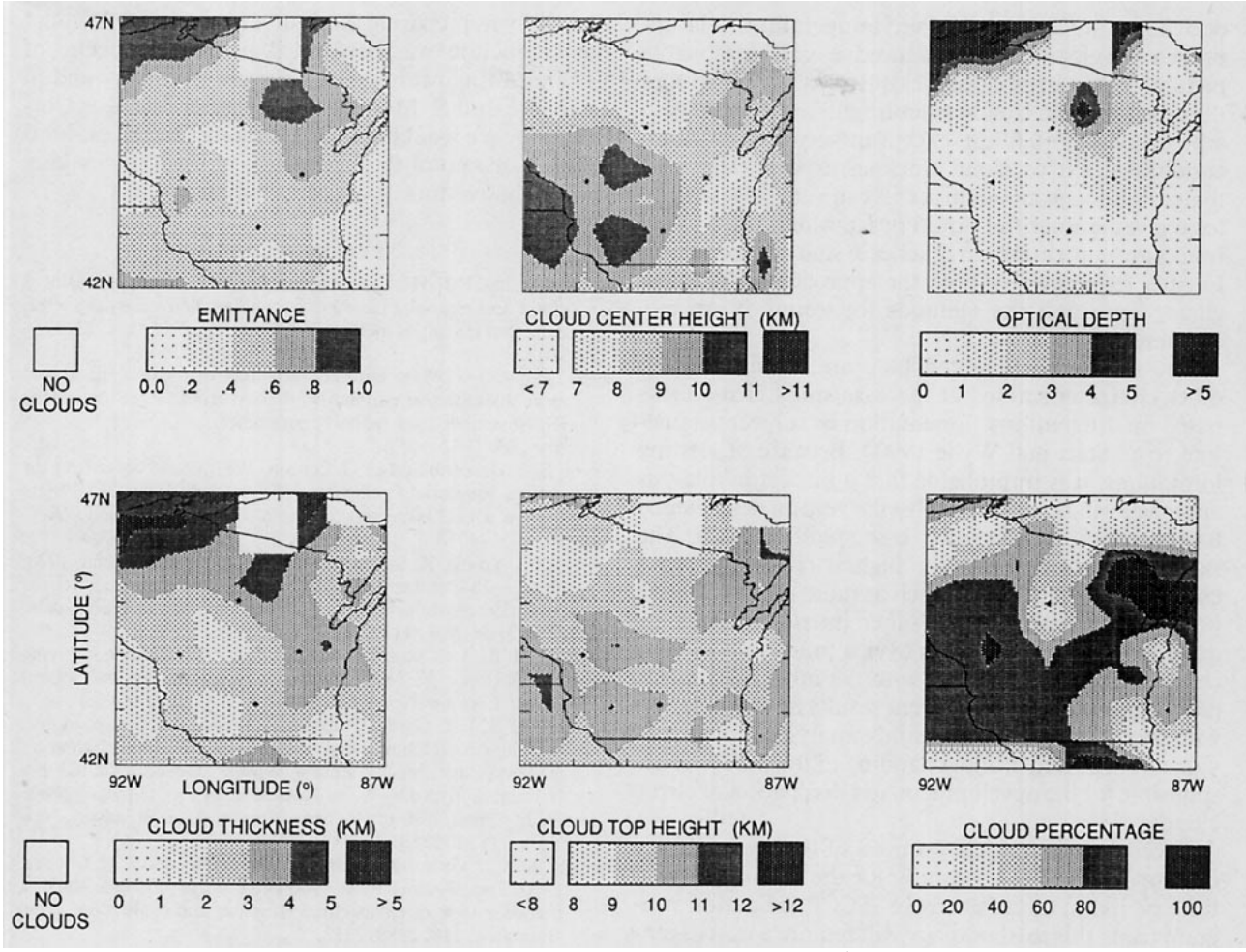

FIG. 24. AVHRR-derived high-cloud parameters for 2100 UTC 28 October 1986.

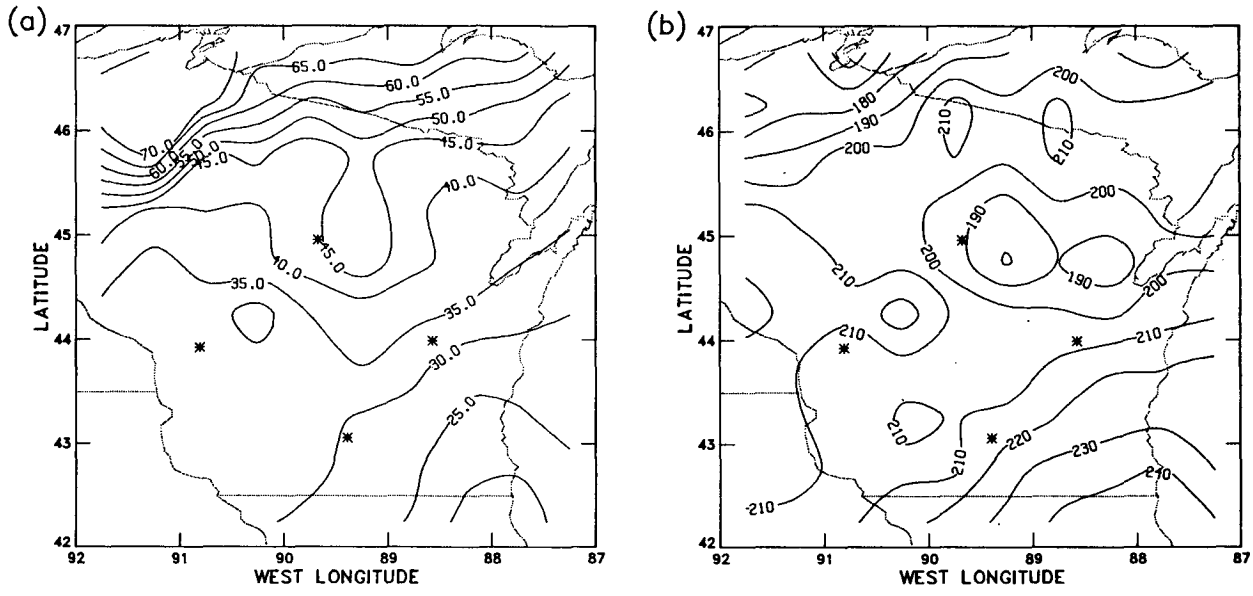

FIG. 25. Broadband radiation components at the top of the atmosphere from the ERBE at 2100 UTC 28 October 1986 (a) albedo in percent; (b) longwave flux in W m^{-2}.

derived emittance and observed temperatures. The approach developed here produced a very reasonable picture of the cirrus cloud fields. It was estimated that the cloud-top and cloud-center heights are derived with a precision of ~0.6 km, except in very broken cloud conditions. Cirrus cloud thicknesses were also estimated. Although cloud thickness can vary substantially for a given amount of liquid or ice water, the derived results are comparable to other case study observations. Further refinement of both the approach for deriving cloud depth and the methods for testing it are recommended.

The results documented here are consistent with other characterizations of the case study cirrus fields based on different instrumentation or subjective analyses (e.g., Starr and Wylie 1990). Because of viewing limitations, it is improbable that a bispectral analysis approach will be able to resolve the vertical detail which has been observed in other case study analyses. The satellite can only detect the highest cloud layer in a column. Satellite analyses such as those presented here, however, complement the other instrumentation by quantifying the cloud fields over a much greater horizontal range than possible with the other instrument platforms. Study of the current results in combination with those from other case study analyses should provide a much deeper understanding of the processes responsible for the development and dissipation of cirrus clouds.

Because the empirical portions of the methodology developed here are valid only for the IFO angles and time period, a comprehensive ISCCP validation program using this methodology will require a tested, generalized version of the analysis techniques. The generalized methodology will take a theoretical approach to computing cloud reflectance since empirical data are not available for enough conditions to model the reflectance at all angles and optical depths. Testing of the generalized version will make use of FIRE's extended-time measurement program and data from future field observations. The ISCCP global products are now available, however, so there is an acute need for immediate implementation of validation studies. Since the cloud parameters derived here are known to a certain degree of precision, the results of this study can be used to perform initial verification of some aspects of the ISCCP products.

Acknowledgments. The assistance of G. G. Gibson and D. F. Young of Lockheed Engineering and Sciences Company in preparing the figures is appreciated. Initial data reduction was performed by R. J. Wheeler of Lockheed Engineering and Sciences Company and S. Eckhause and S. Morgan of Computer Sciences Corporation. We would also like to thank Drs. K. N. Liou and Y. Takano of the University of Utah for making their radiative transfer model available.

REFERENCES

Minnis, P., and E. F. Harrison, 1984a: Diurnal variability of regional cloud and clear-sky radiative parameters derived from GOES data, Part I: analysis method. *J. Climate Appl. Meteor.*, **23,** 993–1011.

——, and ——, 1984b: Diurnal variability of regional cloud and clear-sky radiative parameters derived from GOES data, Part III: November 1978 radiative parameters. *J. Climate Appl. Meteor.*, **23,** 1032–1051.

——, E. F. Harrison and G. G. Gibson, 1987: Cloud cover over the eastern equatorial Pacific derived from July 1983 ISCCP data using a hybrid bispectral threshold method. *J. Geophys. Res.*, **92,** 4051–4073.

——, D. F. Young, K. Sassen, J. M. Alvarez and C. J. Grund, 1990: The 27–28 October 1986 FIRE Cirrus IFO case study: cirrus parameter relationships derived from satellite and lidar data. *Mon. Wea. Rev.*, **118,** 2402–2425.

Platt, C. M. R., J. C. Scott and A. C. Dilley, 1987: Remote sounding of high clouds, VI. Optical properties of midlatitude and tropical cirrus. *J. Atmos. Sci.*, **44,** 729–747.

Rossow, W. B., L. C. Garder, P. Lu and A. Walker, 1988: International Satellite Cloud Climatology Project (ISCCP), documentation of cloud data. *WCRP* Report WMO/TD-No. 266, 122 pp. [Available from Dr. W. B. Rossow at NASA Goddard Space Flight Center, Institute for Space Studies, 2880 Broadway, New York, NY, 10025.]

Sassen, K., C. J. Grund, J. Spinhirne, M. Hardesty and J. M. Alvarez, 1990: The 27–28 October 1986 FIRE cirrus IFO case study: a five lidar view of cirrus cloud structure and evaluation. *Mon. Wea. Rev.*, **118,** 2288–2312.

Smith, G. L., R. N. Green, E. Raschke, L. M. Avis, J. T. Suttles, B. A. Wielicki and R. Davies, 1986: Inversion methods for satellite studies of the Earth's radiation budget: development of algorithms for the ERBE mission. *Rev. Geophys.*, **24,** 407–421.

Starr, D. O'C., 1987: A cirrus-cloud experiment: intensive field observations planned for FIRE. *Bull. Amer. Meteor. Soc.*, **68,** 119–124.

——, and D. P. Wylie, 1990: The 27–28 October 1986 cirrus IFO case study: meteorology and cloud fields. *Mon. Wea. Rev.*, **118,** 2259–2287.

Stowe, L. L., C. G. Wellemeyer, T. F. Eck, H. Y. M. Yeh and The Nimbus-7 Cloud Data Processing Team, 1988: Nimbus-7 global cloud climatology, Part I: algorithms and validation. *J. Climate,* **1,** 445–470.

Takano, Y., and K. N. Liou, 1989a: Radiative transfer in cirrus clouds: I. Single-scattering and optical properties of hexagonal ice crystals. *J. Atmos. Sci.*, **46,** 1–20.

——, and ——, 1989b: Radiative transfer in cirrus clouds: II. Theory and computation of multiple scattering in an anisotropic medium. *J. Atmos. Sci.*, **46,** 21–38.

(continued from p. 2448)

NOTES AND CORRESPONDENCE